Progress In Electromagnetics Research, PIER 43, 181–237, 2003

RIGOROUS COUPLED WAVE ANALYSIS OF BIPOLAR CYLINDRICAL SYSTEMS: SCATTERING FROM INHOMOGENEOUS DIELECTRIC MATERIAL, ECCENTRIC, COMPOSITE CIRCULAR CYLINDERS

J. M. Jarem

Electrical and Computer Engineering Department
University of Alabama in Huntsville
Huntsville, AL 35899, USA

Abstract—Rigorous Coupled Wave Analysis (RCWA) in bipolar coordinates for the first time is used to study electromagnetic (EM) scattering from eccentric, circular, multi-cylinder systems for which spatially, non uniform material (dielectric permittivity) occupies the regions between the interfaces of the cylinders. The bipolar RCWA algorithm presented herein consists of three basic steps which are; (1) solving Maxwell's equations in bipolar coordinates using a state variable (SV) formulation; (2) solving Maxwell's equations in the spatially uniform regions exterior to the inhomogeneous scattering object in terms of circular, cylindrical Bessel-Hankel functions; and (3) enforcement of EM boundary matching equations which leads to a final matrix equation solution of the system. In the paper extensive use of the residue theorem of complex variable theory was made in order to find fast and exact evaluations of the EM boundary interaction integrals that arose between the bipolar, SV solutions and the Hankel-Bessel solutions.

In this paper very extensive reliance on the work of A. A. Kishk, R. P. Parrikar and A. Z. Elsherbeni [22] who studied EM scattering from uniform material multi-eccentric circular cylinders (called herein the KPE algorithm) was made in order to validate the numerical results of the bipolar RCWA algorithm. In this paper, two important system transfer matrices, called the Bessel transfer matrix (based on the KPE algorithm) and called the bipolar SV transfer matrix, were developed in order to validate the numerical accuracy of the RCWA algorithm. The Bessel and SV transfer matrices were very useful for validation purposes because, from the way they were both formulated, they could be meaningfully compared to one another, matrix element to matrix element.

In the paper extensive numerical results are presented for EM scattering from spatially uniform and non uniform multi-eccentric, composite cylinder systems, including calculation of three dimensional plots of the electric and magnetic fields and including calculation of the back and bistatic scattering widths associated with the scattering systems. Also included are three tables of data documenting peak and RMS errors that occur between the KPE and RCWA algorithms when the number of modes are changed, the number of layers in the RCWA algorithm are varied and when the angle of incidence is varied.

1. INTRODUCTION

An important problem in the area of EM spectral domain analysis is the problem of using rigorous coupled wave analysis (RCWA) to determine the EM fields that result when an EM wave is incident on an inhomogeneous material object, that is one whose dielectric permittivity and magnetic permeability parameters are functions of position. The RCWA algorithm which was originally designed to study scattering from planar diffraction gratings [1–9], has been used to study scattering from inhomogeneous objects when the inhomogeneous object was a phi dependent circular cylinder [10–13], when the circular cylinder was an anisotropic permeability [14], when the object was a lossy biological material [15], when the object was an elliptical inhomogeneous cylinder [16, 17], and when the scattering object was an inhomogeneous sphere [18, 19]. A recent book [20] describes the RCWA method and its application to scattering from inhomogeneous objects.

A limitation of work of [13–15] was that it described circular cylindrical materially inhomogeneous systems for which the interior and exterior circular cylinders of the scattering object were concentric. This is a limitation because scattering objects which have a significantly off center material inhomogeneity cannot easily be analyzed in a concentric circular cylindrical system. Although scattering objects with eccentric, cylindrical inhomogeneity can still be theoretically studied as an inhomogeneous object in a centered cylindrical system, if the difference in material values of eccentric material object was large, a very high number of Fourier harmonics would be required to achieve accurate numerical results. The purpose of the present paper therefore will be to further extend the RCWA method to describe EM scattering from inhomogeneous material objects which are comprised of eccentric, circular, multi-cylinder systems for which spatially, nonuniform material (the dielectric permittivity) occupies the regions between the interfaces of the cylinders. This analysis will be carried out in bipolar coordinates (see Figs. 1 and 2) since the coordinates u and v and interfocal parameter a of this coordinate system [21] can be chosen to define the off center exterior and interior boundaries of the scattering object.

The study of EM scattering from an object which is composed of N non concentric, completely enclosed, circular cylinders of radius $r_1 > r_2 >, \ldots, > r_N$ where the material parameters of dielectric permittivity and magnetic permeability are homogeneous (or non varying with spatial position) between the adjacent circular boundaries $r_j > r_{j+1}, j = 1, \ldots, N-1$, has been studied and solved by A. A. Kishk, R. P. Parrikar and A. Z. Elsherbeni [22]. This method will be referred to as the KPE algorithm of [22] herein. By completely enclosed it is meant that cylinder r_1 completely encloses cylinder r_2 which completely encloses cylinder r_3, etc.. The solution of this problem by the KPE algorithm [22] is extremely important to the present work for two reasons. First, the study of EM scattering from eccentric, circular, multi-cylinder systems by the KPE method [22] provides many, very good examples for which the bipolar RCWA algorithm may be validated and tested against with respect to numerical accuracy and convergence. Fig. 1 shows the general bipolar geometry and Fig. 2 shows a specific scattering example involving three eccentric enclosed cylinders which will be studied extensively in the present work. In Fig. 2 the interior and exterior cylinders have the same bipolar coordinates as Fig. 1. One notices from Fig. 2 that because of the geometry and conditions stated earlier, that the solution of the EM scattering problem displayed in this figure is exactly amenable to an exact solution by the KPE algorithm [22] in the case when the material regions between cylinder interfaces are uniform ($\Delta\varepsilon = 0$ in Fig. 2). On the other hand, picking the inner and outer circular cylinder boundaries as the interior ($u = u_0 = 2.211$) and exterior ($u = u_L = 1.551$) interfaces of the bipolar scattering geometry (see Fig.

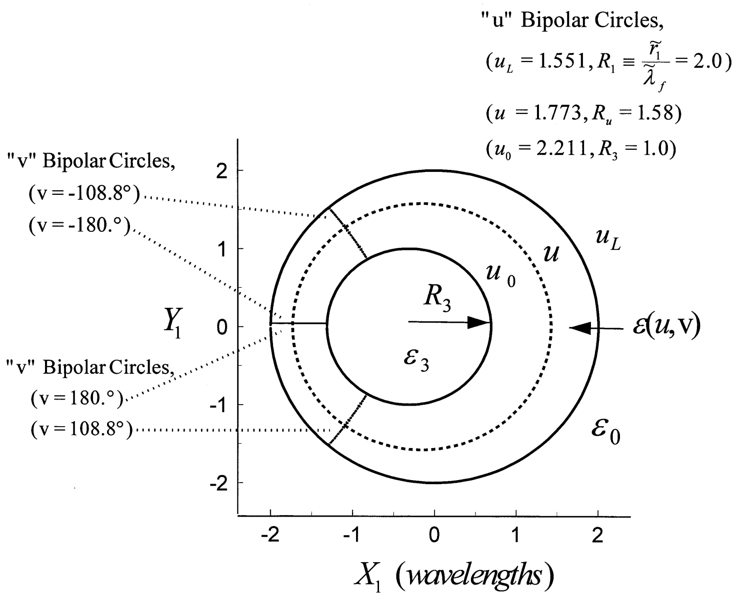

Figure 1. The geometry of the combined bipolar, cylindrical, rectangular coordinate system of the paper is shown. The inhomogeneous region which is described by bipolar coordinates, is divided into L thin layers with interfaces located at $u = u_\ell$, $\ell = 0, \ldots, L$ with the innermost layer at $u = u_0$ and outermost at $u = u_L$. The X_1, Y_1 rectangular coordinate system shown is centered on the outer R_1, $u = u_L$ circle. The figure corresponds to the main scattering example of the paper (see Fig. 2) and the figure is drawn to the exact scale of the numerical values displayed. The interfocal distance $a = \tilde{k}_f \tilde{a} = 28.32451318$. X_1 (*wavelengths*), here and in Figs. 2–9, and Y_1 (*wavelengths*) in Figs. 3–9 represent the number of wavelengths (positive or negative) from the origin. ($X_1 = \tilde{x}_1/\tilde{\lambda}_f$, $Y_1 = \tilde{y}_1/\tilde{\lambda}_f$ are dimensionless.)

1), the middle circular cylinder of Fig. 2 represents an inhomogeneous, uniform-step profile for the RCWA algorithm, if the bulk, relative dielectric permittivities ε_1 and ε_2 are different from one another. To clarify this statement, if the $u = 1.773$ bipolar circle of Fig. 1 (middle u circle) is placed in Fig. 2, and one traces the dotted circle from $v = -180°$ to $v = 0°$, one would first be in Reg. 2 ($\varepsilon(u,v) = \varepsilon_2$), then for some v value ($v = -108.8°$ for $u = 1.773$) cross over to Reg. 1 $\varepsilon(u,v) = \varepsilon_{f1}$. Going from Reg. 2 ($\varepsilon_2$) to Reg. 1 ($\varepsilon_{f1}$) represents the step profile for the range $-180° \leq v \leq 0°$. Because it is necessary to use a

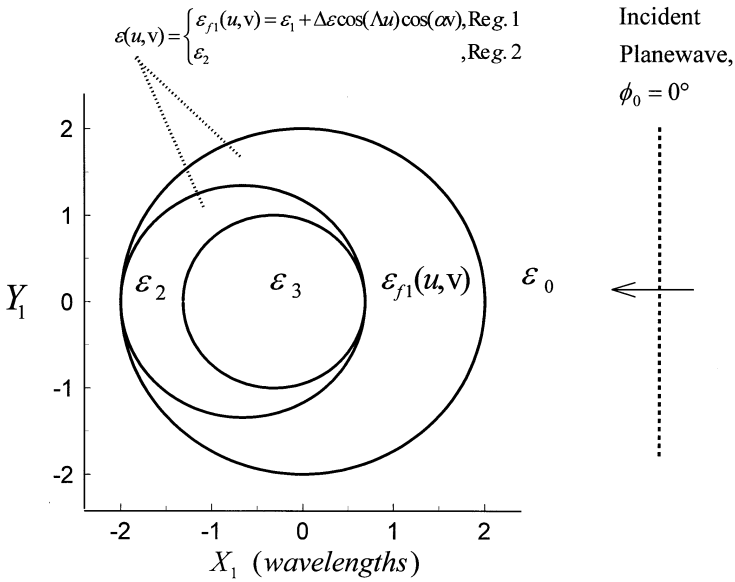

Figure 2. The geometry of the main scattering example of the paper is shown. The relative bulk permittivities in Regs. $0, 1, 2, 3$ which are displayed in the figure are assumed to have values $\varepsilon_0 = 1$, $\varepsilon_1 = 2$, $\varepsilon_2 = 3$, $\varepsilon_3 = 4$. The direction of the $\phi_0 = 0°$ incident planewave is shown. The $\phi_0 = 180°$ incident planewave (not shown) would impinge of the scattering object from the from the left side of figure. In the case when $\Delta\varepsilon = 0$, the permittivity inside Reg. 1 and Reg. 2 is uniform, and this case thus represents a case for which the KPE algorithm [22] can find an exact solution.

Fourier series to represent this step profile, this type of inhomogeneity provides a severe test of the RCWA algorithm since the Fourier series of step profiles tends to converge slowly and have a high spectral content.

The second reason the study of this problem by the KPE algorithm [22] is useful is because the KPE method [22] after a small amount of mathematical manipulation (Appendix B), can be placed in an algebraic form for which a direct numerical comparison of the system transfer matrices as result using the KPE method [22] and as using the bipolar RCWA method can be made. The transfer matrices were useful for validation purposes because, from the way they were both formulated, they could be meaningfully compared to one another, matrix element to matrix element.

This problem of scattering from inhomogeneous eccentric circular, cylindrical composite objects is important, for example in the areas of bioelectromagnetics [15], (where one might want to know EM field levels in biological materials (for example EM field penetration in a limb or torso); terrain clutter where one might want to model EM scattering from eccentric, cylindrical shaped vegetation; study of inhomogeneous radar absorbing materials (RAM); as an exact or approximate solution to validate other mathematical methods; and many other applications as well. It is felt that the work to be presented, could be particularly important to validation of other EM methods (i.e., finite element method (FEM), finite difference-finite time (FD-TD), method of moments (MoM), etc.), since eccentric circular cylindrical systems which possess non spatially uniform material between the interfaces of the cylinders (for example, please see Figs. $2, 3$b, and 3c, $\Delta\varepsilon \neq 0$, of this paper) present a nontrivial scattering geometry (which thus requires non spatially uniform gridding) for which to test the given algorithm (i.e., FEM, FD-TD, MoM).

The analysis to be presented assumes that source excitation and scattering objects are symmetric with respect to the y coordinate (see Figs. 1 and 2). The extension of the RCWA algorithm to the case where the EM fields and a scattering object have arbitrary symmetry is straight forward.

2. RCWA BIPOLAR COORDINATE FORMULATION

This paper is concerned with the problem of determining the EM fields that arise when a plane wave excites EM fields in an inhomogeneous, bipolar system as shown in Figs. 1 and 2. The EM analysis will be carried out by solving Maxwell's equations in all regions and then matching EM boundary conditions at the interfaces. We will use a combination of rectangular, cylindrical and bipolar coordinates to represent the position of all field variables in the paper, and then normalize these coordinates which are in meters, with respect to either the free space wavenumber $\tilde{k}_f$ when presenting equations (i.e., $x = \tilde{k}_f\tilde{x}$, $y = \tilde{k}_f\tilde{y}$, etc., where $\tilde{k}_f = 2\pi/\tilde{\lambda}_f$ and where $\tilde{\lambda}_f$ is free space wavelength) or when displaying graphical results, normalizing them to the free space wavelength $\tilde{\lambda}_f$ (i.e., $X \equiv x/2\pi$, $Y \equiv y/2\pi$, etc.). The bipolar coordinates which are used in this paper to represent the inhomogeneous region shown in Fig. 1 are defined by an interfocal distance $a = \tilde{k}_f\tilde{a}$ [21], a "radial" angular coordinate $u\,(-\infty < u < \infty)$ and an angular coordinate $v\,(-\pi \leq v \leq \pi)$. The rectangular coordinates x, y are the related to bipolar coordinates u, v

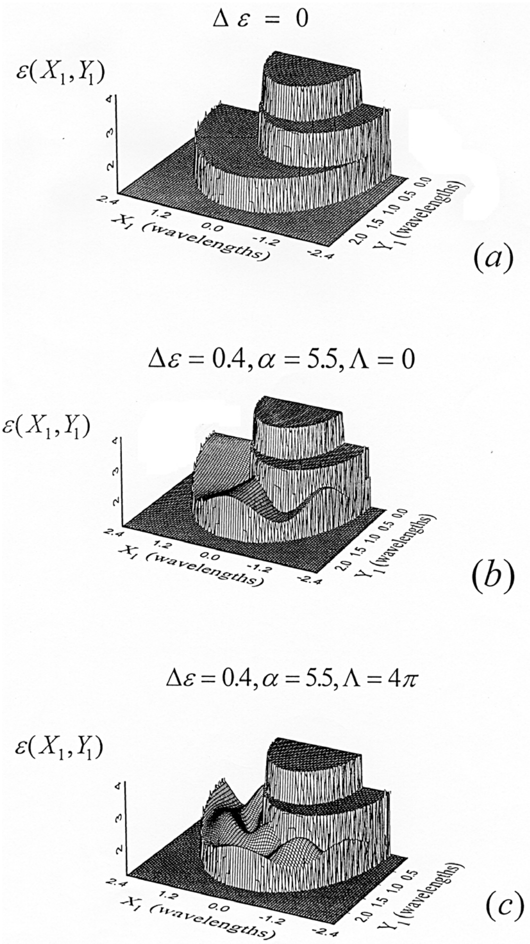

Figure 3. Figs. a, b, and c show the relative dielectric permittivity function of $\varepsilon(X_1, Y_1)$ (from $\varepsilon(u, v)$ of Eq. (89)) as a function of the rectangular coordinates X_1, Y_1 for the parameters listed in each figure.

and interfocal distance a by the equations

$$x = \frac{a\sinh(u)}{\cosh(u) - \cos(v)}, \quad y = \frac{-a\sin(v)}{\cosh(u) - \cos(v)} \tag{1}$$

These equations have been obtained from [21], with the minor modification that the angular bipolar coordinate used in [21] (call it v' in [21] for the moment), was defined on the interval $0 \le v' \le 2\pi$ in [21], whereas herein, the angular coordinate v is defined on the interval

$-\pi \leq v \leq \pi$. Thus the coordinate v' of [21] and the coordinate v used here are related by $v = v' - \pi$. Substitution of $v = v' - \pi$ in Eq. (1) gives the bipolar coordinate formulas used in [21]. As mentioned in the Introduction we assume that the system is symmetric with respect to y coordinate. In bipolar coordinates, the locus of points defined by setting the "radial" coordinate to a constant value u with $-\pi \leq v \leq \pi$, traces out a circle whose center is on the x-axis at $x_{cu} = a/\tanh(u)$ and whose radius is $r_u = a/\sinh(|u|)$. When $u \to \pm\infty$ the circle of constant u's center approaches the interfocal points $x = \pm a$ respectively and the radius of this circle r_u approaches zero. In bipolar coordinates, the locus of points defined by setting the angular coordinate to a constant value v with $-\infty < u < \infty$, traces out a circle whose center is on the y-axis at $y_{cv} = -a/\tan(v)$ and whose radius is $r_v = a[1 + \cot^2(v)]^{1/2}$. All circles of constant v pass through both interfocal points $x = \pm a$. In bipolar coordinates the scale factors of the system are for the u, v coordinates defined here are given by

$$h_u(u, v) = h_v(u, v) = h(u, v) \equiv \frac{a}{\cosh(u) - \cos(v)} \tag{2}$$

Ref. [21] shows a complete geometry of bipolar coordinates u and v'.

Fig. 1 shows the rectangular, cylindrical and bipolar coordinates of a general type of scattering example that one might solve using the bipolar RCWA algorithm whereas Fig. 2 shows the details of the particular scattering example that we will be most concerned with in this paper. Figs. 1 and 2 are drawn to the exact scale of the scattering examples which will be presented in the paper. In this paper we use bipolar coordinates to describe the inhomogeneous region of the scattering object and we use the eccentric, circular, cylindrical coordinate system used by KPE [22] ($\rho_j, \phi_j,\ j = 1, 3$ with the origin O_j at the center of each eccentric cylinder in Fig. 1) to describe the EM fields and geometry outside the inhomogeneous region. The interfaces shown in Fig. 2 satisfy $\rho_j = r_j,\ r_j = \tilde{k}_f \tilde{r}_j,\ R_j = r_j/2\pi,\ j = 1, 2, 3$. In applying the RCWA algorithm to the geometry of Fig. 1, it is assumed that the inhomogeneous region displayed there, is divided into L thin layers of uniform width and that the interfaces of the thin layers are located on the circles at $u_\ell = u_0 - \ell\Delta u,\ \ell = 0, 1, \ldots, L$, where $\Delta u = (u_0 - u_L)/L > 0$, where $u = u_0$ is located on the circle $\rho_3 = r_3$ and where $u = u_L$ is located on the circle $\rho_1 = r_1$. In Figs. 1 and 2 the rectangular coordinates $X_1 = x_1/2\pi,\ Y_1 = y_1/2\pi$, which are centered on the scattering objects exterior boundary interface $\rho_1 = r_1$ $(u = u_L)$, are related to the bipolar rectangular coordinates of Eq. (1) by the relations $x_1 = x - x_1^c,\ y_1 = y$ where $x_1^c = a/\tanh(u_L)$. In Figs. 1 and 2 the exterior boundary has a radius $r_1 = a/\sinh(u_L)$ and the interior boundary a radius $r_3 = a/\sinh(u_0)$ with $r_3 < r_1$. The rectangular coordinates, call them $x_u(u,v)$, $y_u(u,v)$, whose origin is located at the center of a circle of constant u, call it O_u, are related to the rectangular coordinates $x(u,v)$, $y(u,v)$, of Eq. (1) by the relations $x_u(u,v) = x(u,v) - x_{cu}$, $y_u(u,v) = y(u,v)$ where $x_{cu} = a/\tanh(u)$. The cylindrical coordinates, call them $\rho_u(u,v)$, $\phi_u(u,v)$, whose origin is located at O_u, are related to $x(u,v)$ and $y(u,v)$ coordinates Eq. (1) of the overall coordinate system, by the cylindrical coordinate relations

$$\rho_u(u,v) = \sqrt{x_u^2(u,v) + y_u^2(u,v)}, \ \phi_u(u,v) = \tan^{-1}(y_u(u,v)/x_u(u,v)) \tag{3}$$

Please note $\rho_u(u,v) = r_u = a/\sinh(|u|)$.

The EM solution in the inhomogeneous dielectric region, following the procedure in [16, 17, 20], is obtained by solving Maxwell's equations in bipolar coordinates by a state variable approach in each thin layer $u_{\ell+1} \le u \le u_\ell$, $\ell = 0, \ldots, L-1$. Making the substitutions $U_{hu}(u,v) = \tilde{\eta}_f h(u,v) H_u(u,v)$, and $U_{hv}(u,v) = \tilde{\eta}_f h(u,v) H_v(u,v)$ where $H_u(u,v)$ and $H_v(u,v)$ represent the magnetic fields in each thin shell region, $\tilde{\eta}_f = 377\,\Omega$, we find that Maxwell's equations in each bipolar, cylindrical shell are given by

$$\frac{\partial E_z(u,v)}{\partial v} = -j\mu U_{hu}(u,v) \tag{4}$$

$$\frac{\partial E_z(u,v)}{\partial u} = j\mu U_{hv}(u,v) \tag{5}$$

$$\frac{\partial U_{hv}(u,v)}{\partial u} - \frac{\partial U_{hu}(u,v)}{\partial v} = j\varepsilon(u,v) h^2(u,v) E_z(u,v) \tag{6}$$

In these equations $\varepsilon(u,v)$ represents the inhomogeneous relative permittivity in the inhomogeneous region (shown in Fig. 1).

To solve Eqs. (4)–(6), we expand in the Floquet harmonics $-\pi \le v \le \pi$:

$$\begin{aligned}
E_z(u,v) &= \sum_{i=-\infty}^{\infty} S_{zi}(u) \exp(jiv), \\
U_{hu}(u,v) &= \sum_{i=-\infty}^{\infty} U_{hui}(u) \exp(jiv), \\
U_{hv}(u,v) &= \sum_{i=-\infty}^{\infty} U_{hvi}(u) \exp(jiv), \\
\varepsilon_h(u,v) E_z(u,v) &= \sum_{i=-\infty}^{\infty} \left[\sum_{i'=-\infty}^{\infty} \varepsilon_{h,i-i'} S_{zi'} \right] \exp(jiv),
\end{aligned}$$

$$\varepsilon_h(u,v) \equiv \varepsilon(u,v)h^2(u,v) = \sum_{i=-\infty}^{\infty} \varepsilon_{hi}(u)\exp(jiv) \tag{7}$$

If these expansions are substituted in Eqs. (4)–(6), and after letting $\underline{S_z}(u) = [S_{zi}(u)]$, $\underline{U_{hu}(u)} = [U_{hui}(u)]$, and $\underline{U_{hv}(u)} = [U_{hvi}(u)]$ be column matrices and letting $\underline{\underline{I}} = [\delta_{i,i'}]$, $\underline{\underline{\varepsilon_h(u)}} = [\varepsilon_{h,i,i'}(u)]$, $\varepsilon_{h,i,i'}(u) = \varepsilon_{h,i-i'}(u)$, $\underline{\underline{K}} = [iK\delta_{i,i'}]$, $K = 2\pi/\Lambda_v$, $\Lambda_v = 2\pi$ (Λ_v may be called the v-angular grating period and $\delta_{i,i'}$ is the Kronecker delta) be square matrices, we find after manipulation [16, 17, 20]

$$\frac{\partial \underline{V}}{\partial u} = \underline{\underline{A}}\,\underline{V}, \quad \underline{V} = \begin{bmatrix} \underline{S_z^e(u)} \\ \underline{U_{hv}^e(u)} \end{bmatrix}, \quad \underline{\underline{A}} = \begin{bmatrix} \underline{\underline{A_{11}}} & \underline{\underline{A_{12}}} \\ \underline{\underline{A_{21}}} & \underline{\underline{A_{22}}} \end{bmatrix} \tag{8}$$

where

$$\underline{\underline{A_{11}}} = 0, \quad \underline{\underline{A_{12}}} = j\mu\underline{\underline{I}}, \quad \underline{\underline{A_{21}}} = j\left[\underline{\underline{\varepsilon_h}} - \frac{1}{\mu}\underline{\underline{K}}^2\right], \quad \underline{\underline{A_{22}}} = 0 \tag{9}$$

After truncating Eqs. (8), (9) with $i = -I, \ldots, I$, one may determine the eigenvalues and eigenvectors of the matrix $\underline{\underline{A}}$ and thus obtain a SV solution in each thin layer of the system.

An alternate equation for the SV analysis, as presented in [6] and [7] (and as reviewed and discussed in [20]) for planar diffraction gratings, is to reduce Eq. (8) to a second order differential matrix equation and perform an eigenanalysis of the resulting equations. Following this procedure we have, for a given thin layer,

$$\frac{d}{du}\underline{S_z^e} = \underline{\underline{A_{12}}}\,\underline{U_{hv}^e}, \qquad \frac{d}{du}\underline{U_{hv}^e} = \underline{\underline{A_{21}}}\,\underline{S_z^e} \tag{10}$$

or

$$\frac{d^2}{du^2}\underline{S_z^e} = \underline{\underline{A_{12}}}\,\underline{\underline{A_{21}}}\,\underline{S_z^e} \tag{11}$$

Letting

$$\underline{S_z^e(u)} = \underline{S_z(u_\ell)}\exp(qu') \tag{12}$$

where $u' = u - u_\ell \le 0$, $u_{\ell+1} \le u \le u_\ell$, $\ell = 0, \ldots, L-1$, letting $\underline{\underline{C}} = -\underline{\underline{A_{12}}}\,\underline{\underline{A_{21}}}$, we find after substituting Eq. (11) into Eq. (12) and differentiating that

$$\underline{\underline{C}}\,\underline{S_z^e} = Q\underline{S_z^e} \tag{13}$$

where $Q \equiv -q^2$. When taking into account the symmetry with respect to the y-axis as discussed earlier, it was found that $I+1$ distinct eigenvalues and eigenvectors were associated with the matrix

$\underline{\underline{C}}$ and it was also found that the eigenvalues Q_n were purely real, with some of them assuming positive values and some them assuming negative values. In the present work the eigenvalues (and eigenvectors associated with Q_n) were ordered for each thin layer, such that $Q_1 > Q_2 > \ldots$. Positive values of the eigenvalue Q_n correspond to propagating eigenmodes (since $q_n^2 = -Q_n$) and negative values of Q_n correspond to nonpropagating or evanescent modes.

Letting $Q_{n\ell}$ and $\underline{S_{zn\ell}}$ (with the subscript ℓ now included) be the eigenvalues and eigenvectors at $u = u_\ell$, $\ell = 0, \ldots, L-1$ of the matrix $\underline{\underline{C_\ell}}$ (i.e., $\underline{\underline{C_\ell}}\,\underline{S_{zn\ell}} = Q_{n\ell}\underline{S_{zn\ell}}$), we find that there are two matrix eigensolutions of the original SV matrix $\underline{\underline{A}}$ of Eq. (8) which may be expressed in terms of the just mentioned eigenvalues and eigenvectors $Q_{n\ell}$ and $\underline{S_{zn\ell}}$. The electric field and magnetic field portions of these matrix eigensolutions are given by

$$\begin{aligned}
\underline{S_{zn\ell}^{e+}(u')} &= \underline{S_{zn\ell}}\exp\left(-\sqrt{-Q_{n\ell}}u'\right) \equiv \underline{S_{zn\ell}}\exp(-q_{n\ell}u') \\
\underline{U_{hvn\ell}^{e+}(u')} &= \frac{1}{j\mu}\frac{\partial \underline{S_{zn\ell}^{e+}(u')}}{\partial u'} = -Z_{n\ell}\underline{S_{zn\ell}^{e+}(u')} \\
\underline{S_{zn\ell}^{e-}(u')} &= \underline{S_{zn\ell}}\exp\left(\sqrt{-Q_{n\ell}}u'\right) \equiv \underline{S_{zn\ell}}\exp(q_{n\ell}u') \\
\underline{U_{hvn\ell}^{e-}(u')} &= \frac{1}{j\mu}\frac{\partial \underline{S_{zn\ell}^{e-}(u')}}{\partial u'} = Z_{n\ell}\underline{S_{zn\ell}^{e-}(u')}
\end{aligned} \tag{14}$$

where

$$q_{n\ell} = \sqrt{-Q_{n\ell}} = \begin{cases} j\sqrt{Q_{n\ell}}, & Q_{n\ell} \geq 0 \\ \sqrt{-Q_{n\ell}}, & Q_{n\ell} < 0 \end{cases} \tag{15}$$

$$Z_{n\ell} = \frac{q_{n\ell}}{j\mu} \tag{16}$$

where $u' = u - u_\ell \leq 0$, $u_{\ell+1} \leq u \leq u_\ell$, $\ell = 0, \ldots, L-1$. The eigenmodes (or eigenfunctions) at $u = u_\ell$ (or $u' = 0$) associated with the eigenvalues and eigenvectors $Q_{n\ell}$ and $\underline{S_{zn\ell}}$ of the matrix $\underline{\underline{C_\ell}}$ respectively, are obtained by summing the Fourier coefficients contained in the matrix $\underline{S_{zn\ell}} = [S_{zin\ell}]$ and are given by

$$S_{zn\ell}(v) = \sum_{i=-I}^{I} S_{zin\ell}\exp(jiv) \tag{17}$$

These eigenmodes which have been normalized to unity, were found numerically to satisfy the orthogonality relation

$$\int_{-\pi}^{\pi} S_{zn\ell}(v) S_{zn'\ell}(v) dv = \delta_{n,n'} \tag{18}$$

where $(n, n') = 1, \ldots, N$ and N is the number of orthogonal eigenmodes under consideration to a high degree of accuracy. This orthogonality relation proved to be very helpful for enforcing EM boundary conditions at different thin layer interfaces and at the interior and exterior boundaries of the system. We note at this point, that when using the eigensolutions of Eq. (17) to either expand unknown EM fields or using them to enforce EM boundary conditions at the interfaces of the system, that it is not necessary to always use the full set of $n = 1, \ldots, I+1$ eigenfunctions which are available from the eigen matrix analysis, but if one desires, one may use a smaller set with $N < I + 1$. Using a set of eigensolutions with $N < I + 1$, may be useful as one then avoids using the highest order modes which may suffer truncation error. Or put another way, if it is desired to use N orthogonal modes of a given accuracy, one may use a larger I truncation order to generate those N orthogonal modes.

An important requirement of the bipolar RCWA formulation concerns the fast and accurate numerical calculation of the Fourier series coefficients $\varepsilon_{hi}(u)$ in Eq. (7). Fast calculations of $\varepsilon_{hi}(u)$ are needed because the bipolar SV solution must be found separately in a possibly large number L of thin layers, and accurate calculation of the Fourier harmonics of $\varepsilon_{hi}(u)$ is needed because these Fourier coefficients are used to form the SV matrices of Eqs. (8), (9). Inaccurate matrix values SV matrices will naturally lead to inaccurate and incorrect SV solutions. It turns out that in the present paper that the Fourier coefficients $\varepsilon_{hi}(u)$ can be calculated almost exactly provided that the Fourier coefficients of the inhomogeneous $\varepsilon(u, v)$ can be calculated exactly (for example, in this paper, Figs. 2 and 3 corresponds to $\varepsilon(u, v)$ step-cosine profiles which can be done exactly). This follows because the Fourier coefficients of the $h^2(u, v)$ function can be calculated exactly using the residue theorem of complex variable theory [23] and thus the $\varepsilon_{hi}(u)$ Fourier coefficients of the product $\varepsilon_h(u, v) \equiv \varepsilon(u, v)h^2(u, v)$ can be calculated from a discrete Fourier convolution of the Fourier coefficients of the two product functions $\varepsilon(u, v)$ and $h^2(u, v)$. Details of the determination of the Fourier coefficients of $h^2(u, v)$ by the residue theorem are given in Appendix A.

We will now present the EM fields in the Regs. 0 and 3 (shown in Figs. 1 and 2) which are outside of the inhomogeneous material region of the scattering object and which are assumed to have spatially uniform relative permittivities ε_0 and ε_3 respectively. In these regions we will use exactly the same coordinates and Bessel functions EM field expansions as were by KPE [22], but specialized to the symmetric problem under consideration. In Reg. 3 the electric and magnetic fields are given by in general

$$\begin{aligned}
E_z^{(3)}(\rho_3,\phi_3) &= \sum_{m'=0}^{N-1}\left\{A_{m'}^{(3)}J_{m'}(k_3\rho_3)+B_{m'}^{I}H_{m'}^{(2)}(k_3\rho_3)\right\}\cos(m'\phi_3)\\
&\equiv \sum_{m'=0}^{N-1}E_{m'}^{(3)}(\rho_3)\cos(m'\phi_3) \qquad (19)\\
\tilde{\eta}_f H_{\phi_3}^{(3)}(\rho_3,\phi_3) &\equiv U_{\phi_3}^{(3)}(\rho_3,\phi_3)\\
&= \sum_{m'=0}^{N-1}\left\{\left[\frac{k_3}{j\mu_3}\right]\left[A_{m'}^{(3)}J'_{m'}(k_3\rho_3)+B_{m'}^{I}H_{m'}^{(2)'}(k_3\rho_3)\right]\right\}\\
&\quad\cdot\cos(m'\phi_3)\\
&\equiv \sum_{m'=0}^{N-1}U_{m'}^{(3)}(\rho_3)\cos(m'\phi_3), \qquad \rho_{s3}<\rho_3\le r_3 \qquad (20)
\end{aligned}$$

where $\tilde{\eta}_f = 377\Omega,\ k_3 = \sqrt{\mu_3\varepsilon_3},\ \mu_3 = \mu_0 = 1$ and where it is assumed that ρ_{s3} encloses a symmetric source which gives rise to the symmetric incident field which is associated with the $B_{m'}^{I}$ coefficients. In Reg. 0 the EM fields are given by

$$\begin{aligned}
E_z^{(1)}(\rho_1,\phi_1) &= \sum_{m'=0}^{N-1}\left\{A_{m'}^{I}J_{m'}(k_0\rho_1)+B_{m'}^{(0)}H_{m'}^{(2)}(k_0\rho_1)\right\}\cos(m'(\phi_1-\phi_0))\\
&\equiv \sum_{m'=0}^{N-1}E_{m'}^{(1)}(\rho_1)\cos(m'\phi_1) \qquad (21)
\end{aligned}$$

$$\begin{aligned}
\tilde{\eta}_f H_{\phi_1}^{(1)}(\rho_1,\phi_1) &\equiv U_{\phi_1}^{(1)}(\rho_1,\phi_1)\\
&= \sum_{m'=0}^{N-1}\left\{\left[\frac{k_0}{j\mu_0}\right]\left[A_{m'}^{I}J'_{m'}(k_0\rho_1)+B_{m'}^{(0)}H_{m'}^{(2)'}(k_0\rho_1)\right]\right\}\\
&\quad\cdot\cos(m'(\phi_1-\phi_0))\\
&\equiv \sum_{m'=0}^{N-1}U_{m'}^{(1)}(\rho_1)\cos(m'\phi_1) \qquad (22)
\end{aligned}$$

where $k_0 = \sqrt{\mu_0\varepsilon_0},\ \mu_0 = 1,\ r_1 < \rho_1 \le \rho_{s0}$, where $\phi_0 = 0$ or $\phi_0 = \pi$, (note $\sin m'\phi_0 = 0$) and where it is assumed that a symmetric source which is exterior to ρ_{s0}, that is, $\rho_1 > \rho_{s0}$, gives rise to a symmetric incident field which is associated with the $A^I_{m'}$ coefficients. In this paper we will be concerned with numerical results for which $B^I_{m'}$ will be taken to be zero, for which $\rho_{s0} \to \infty$ and the $A^I_{m'}$ coefficients are taken to those coefficients which correspond to an incident plane wave from the direction where $\phi_0 = 0$ or $\phi_0 = \pi$. In Eqs. (19)–(22) the number of expansion modes in Regs. 0 and 3 has been set equal to the number of SV expansion modes N used in each thin layer.

The EM field solutions in the inhomogeneous region (see Fig. 1) in bipolar coordinates in a small range $-\Delta u \le u' \le 0$ ($\Delta u = \frac{u_0 - u_L}{L} > 0$, $u' = u - u_\ell \le 0$, $u_{\ell+1} \le u \le u_\ell$, $\ell = 0, \ldots, L-1$) (pl. recall that $u = u_0$ corresponds to the inner boundary r_3 and $u = u_L$ corresponds to the outer boundary r_1 (Fig. 1)) using the SV eigenvector EM solutions $\underline{S^{e+}_{zn\ell}(u')}$, $\underline{S^{e-}_{zn\ell}(u')}$, $\underline{U^{e+}_{hvn\ell}(u')}$, and $\underline{U^{e-}_{hvn\ell}(u')}$ of Eqs. (14)–(18) are given by

$$\begin{aligned} E_z^{(2)}(u', u_\ell, v) &= \sum_{n'=1}^{N} \left\{ C^+_{n'\ell} \exp(-q_{n'\ell} u') + C^-_{n'\ell} \exp(q_{n'\ell} u') \right\} S_{zn'\ell}(v) \\ &\equiv \sum_{n'=1}^{N} E_{n'\ell}(u') S_{zn'\ell}(v) \end{aligned} \tag{23}$$

$$\begin{aligned} U_{hv}^{(2)}(u', u_\ell, v) &= \sum_{n'=1}^{N} \left\{ -C^+_{n'\ell} \exp(-q_{n'\ell} u') + C^-_{n'\ell} \exp(q_{n'\ell} u') \right\} Z_{n'\ell} S_{zn'\ell}(v) \\ &\equiv \sum_{n'=1}^{N} U_{hn'\ell}(u') S_{zn'\ell}(v) \end{aligned} \tag{24}$$

where $S_{zn'\ell}(v)$ has been defined in Eq. (17). In these equations $C^+_{n'\ell}$ and $C^-_{n'\ell}$ represent the unknown expansion coefficients in the $u_{\ell+1} \le u \le u_\ell$, $\ell = 0, \ldots, L-1$ thin layer.

Before matching boundary conditions, we would like to relate the cylindrical bipolar coordinate $\phi_u(u, v)$ defined in Eq. (3) to the to the cylindrical coordinates ϕ_1 and ϕ_3 of the Reg. 0 and 3 boundaries respectively. Using Eq. (3) at $u = u_L$ (Reg. 0, exterior boundary) and at $u = u_0$ (Reg. 3, interior boundary) and we have respectively

$$\phi_1(v) = \phi_u(u_L, v) = \tan^{-1}\left[(y(u_L, v)/(x(u_L, v) - x_{cu_L}) \right] \tag{25}$$

$$\phi_3(v) = \phi_u(u_0, v) = \tan^{-1}\left[(y(u_0, v)/(x(u_0, v) - x_{cu_0}) \right] \tag{26}$$

In matching boundary conditions at the exterior and interior boundaries to the inhomogeneous material region, using Eqs. (25), (26), it is important to relate the complicated, cosine functions $\cos(m\phi_1(v))$ and $\cos(m\phi_3(v))$ in Eqs. (19)–(22) to the $\exp(jiv)$ Fourier series expansions which occur in Eqs. (23), (24) (after Eq. (17) has been substituted in Eqs. (23), (24)) in a manner which is as accurate and efficient as possible. This may be accomplished by expressing the exponentials $\exp(\pm jm\phi_1(v))$ and $\exp(\pm jm\phi_3(v))$ which make up the functions $\cos(m\phi_1(v))$ and $\cos(m\phi_3(v))$, respectively, as a complex exponential Fourier series, namely

$$\exp(jp\phi(u,v)) = \sum_{i=-\infty}^{\infty} \alpha_i^{(p)}(u)\exp(jiv) \tag{27}$$

where $p = \pm m$, $u = u_L$ or $u = u_0$, and then determining the exponential Fourier coefficients $\alpha_i^{(p)}(u)$. It turns out that the Fourier coefficients $\alpha_i^{(p)}(u)$ of this series may be calculated exactly using the residue theorem of complex variable theory [23]. Appendix A of this paper gives details on how these coefficients are calculated and what values these coefficients assume.

The objective now is match EM boundary conditions at all interfaces and determine all unknown expansion coefficients of the system as defined by Eqs. (19)–(24). Starting at the $u = u_0$ (r_3 interior boundary) we have using Eqs. (19)–(24)

$$\begin{aligned} E_z^{(2)}(u',u_\ell,v)\Big|_{u_\ell=u_0,u'=0,\ell=0} &= \left[\sum_{n'=1}^{N} E_{n'\ell}(u')S_{zn'\ell}(v)\right]\Big|_{u_\ell=u_0,u'=0,\ell=0} \\ &= E_z^{(3)}(\rho_3,\phi_3)\Big|_{\rho_3=r_3^-} \\ &= \left[\sum_{m'=0}^{N-1} E_{m'}^{(3)}(\rho_3)\cos(m'\phi_3)\right]\Big|_{\rho_3=r_3^-} \end{aligned} \tag{28}$$

$$\begin{aligned} &\left[\frac{-1}{h(u,v)}U_{hv}^{(2)}(u',u_\ell,v)\right]\Big|_{u_\ell=u_0,u'=0,\ell=0} \\ &= \left[\frac{-1}{h(u,v)}\sum_{n'=1}^{N} U_{hn'\ell}(u')S_{zn'\ell}(v)\right]\Big|_{u_\ell=u_0,u'=0,\ell=0} \\ &= U_{\phi_3}^{(3)}(\rho_3,\phi_3)\Big|_{\rho_3=r_3^-} = \sum_{m'=0}^{N-1}\left[U_{m'}^{(3)}(\rho_3)\cos(m'\phi_3)\right]\Big|_{\rho_3=r_3^-} \end{aligned} \tag{29}$$

where $\rho_3 = r_3^-$ means just inside the Reg. 3 interior. The minus sign in Eq. (29) in the square bracket is present because at $\rho_3 = r_3$, $u = u_0$

interface at each point on this circle, the unit vectors $\hat{a}_v(u = u_0)$ and $\hat{a}_{\phi_3}(\rho_3 = r_3)$ are in opposite directions or satisfy $\hat{a}_v(u = u_0) = -\hat{a}_{\phi_3}(\rho_3 = r_3)$ thus opposite signs of the tangential magnetic field components must be included for a correct boundary matching at the interior boundary.

To enforce the electric field boundary condition of Eq. (28) at the $\rho_3 = r_3,\ u = u_0$ interface, Eq. (28) is multiplied on both sides by the weighting or testing functions $\{\cos(m\phi_3)\},\ m = 0, \ldots, N-1$ and then integrated over the range $-\pi \le \phi_3 \le \pi$. This results in the equation

$$\begin{aligned}
&\left[\sum_{n'=1}^{N} E_{n'\ell}(u') \int_{-\pi}^{\pi} S_{zn'\ell}(v)\cos(m\phi_3(v))d\phi_3(v)\right]\Big|_{u_\ell=u_0,u'=0,\ell=0} \\
&= \left[\sum_{m'=0}^{N-1} E_{m'}^{(3)}(\rho_3) \int_{-\pi}^{\pi} \cos(m\phi_3)\cos(m'\phi_3)d\phi_3\right]\Big|_{\rho_3=r_3^-} \\
&= \sum_{m'=0}^{N-1} E_{m'}^{(3)}(r_3)\pi[1+\delta_{m,0}]\delta_{m,m'}
\end{aligned} \tag{30}$$

The integral on the left hand side, after a change of variables on the interior circle $\rho_3 = r_3,\ u = u_\ell|_{\ell=0} = u_0$ from integration with respect to the $\phi_3(v)$ variable (see Eq. (26)) to integration with respect to the v variable, noting that $\phi_3(v)|_{v=\pi} = -\pi$ and $\phi_3(v)|_{v=-\pi} = \pi$ (see Fig. 1), becomes substituting $\ell = 0$ in $S_{zn'\ell}(v)$,

$$Z_{m,n'}^{cE3} = \int_{\pi}^{-\pi} \left[S_{zn'0}(v)\cos(m\phi_3(v))\frac{d\phi_3(v)}{dv}\right] dv \tag{31}$$

This integral and may evaluated exactly by: (1) substituting for $\cos(m\phi_3(v))\frac{d\phi_3(v)}{dv}$ in Eq. (31) the Fourier series ($\rho_3 = r_3,\ u = u_\ell|_{\ell=0} = u_0$)

$$\cos(m\phi_3(v))\frac{d\phi_3(v)}{dv} = \sum_{i=-\infty}^{\infty} \frac{1}{2}\left[\zeta_i^{(m)}(u_0) + \zeta_i^{(-m)}(u_0)\right]\exp(jiv) \tag{32}$$

where the Fourier coefficients $\zeta_i^{(p)}(u)$ are defined by

$$\exp(jp\phi_u(u,v))\frac{d\phi_u(u,v)}{dv} = \sum_{i=-\infty}^{\infty} \zeta_i^{(p)}(u)\exp(jiv) \tag{33}$$

where $p = \pm m$ and where $\phi_3(v)$ is given in Eq. (26); (2) substituting the exponential Fourier series expansion for $S_{zn'\ell}(v),\ \ell = 0$ as defined by

Eq. (17); and (3) integrating, in a straight forward way, the product of the two just described exponential Fourier series over the limits defined by the integral in Eq. (32). The result of the integration is

$$Z^{cE3}_{m,n'} = -\pi \sum_{i=-I}^{I} \left(\zeta_i^{(m)}(u_0) + \zeta_i^{(-m)}(u_0)\right) S_{z,-i,n',0} \tag{34}$$

In Eqs. (32)–(34), the Fourier coefficients $\zeta_i^{(p)}(u)$ of Eq. (33), like the Fourier coefficients $\alpha_i^{(p)}(u)$ of Eq. (27), may be evaluated exactly using the residue theorem, and the details are given in Appendix A. The final electric field equation becomes after substituting $\ell = 0$, evaluating the Knronecker delta function $\delta_{m,m'}$ in Eq. (30),

$$\sum_{n'=1}^{N} Z^{cE3}_{m,n'} E_{n'0}(0) \equiv \sum_{n'=1}^{N} Z^{cE3}_{m,n'} E^{SV3}_{n'} = E^{(3)}_m(r_3^-)\pi[1+\delta_{m,0}] \tag{35}$$

where the coefficient $E^{SV3}_{n'}$ has been defined to be $E^{SV3}_{n'} \equiv E_{n'\ell}(u')|_{u'=0,\rho_3=r_3^+,\ell=0}$, and $E_{n'\ell}(u')$ is defined in Eq. (23). The superscript "$SV3$" in this equation refers to the evaluation of the state variable solution at $u = u_0$ (or $\rho_3 = r_3^+$, where $\rho_3 = r_3^+$ means just inside the inhomogeneous scattering object region).

To enforce the magnetic field boundary condition of Eq. (29) at the $\rho_3 = r_3$, $u = u_0$ interface, Eq. (29) is multiplied on both sides, just as the electric field Eq. (28) was, by the weighting or testing functions $\{\cos(m\phi_3)\}$, $m = 0, \ldots, N-1$ and then integrated over the range $-\pi \le \phi_3 \le \pi$. The resulting equation is

$$\begin{aligned} &\left[\sum_{n'=1}^{N} U_{hn'\ell}(u') \int_{-\pi}^{\pi} \left[\frac{-1}{h(u,v)}\right] S_{zn'\ell}(v)\cos(m\phi_3(v))d\phi_3(v)\right]\Big|_{u=u_0,u'=0,\ell=0} \\ &= \left[\sum_{m'=1}^{N-1} U^{(3)}_{m'}(\rho_3) \int_{-\pi}^{\pi} \cos(m\phi_3)\cos(m'\phi_3)d\phi_3\right]\Big|_{\rho_3=r_3^-} \\ &= \sum_{m'=1}^{N-1} U^{(3)}_{m'}(r_3^-)\pi[1+\delta_{m,0}]\delta_{m,m'} \end{aligned} \tag{36}$$

The integral on the left hand side of Eq. (36) may be evaluated in a similar way as was the integral in Eq. (30). Calling the integral $Z^{cU3}_{m,n'}$, changing variables from ϕ_3 to v, and letting $\ell = 0$ and $u = u_0$ in

Eq. (36), we find that the integral may be written

$$Z^{cU3}_{m,n'} = \int_{\pi}^{-\pi} \left[\frac{-1}{h(u_0,v)}\right] S_{zn'0}(v)\cos(m\phi_3(v))\frac{d}{dv}\phi_3(v)dv \qquad (37)$$

Carrying out the differentiation of $\frac{d}{dv}\phi_3(v)$ and after a small amount of algebra it is found

$$\frac{1}{h(u_0,v)}\frac{d}{dv}\phi_3(v) = \sinh(u_0)/a \qquad (38)$$

Substitution of Eq. (38) in Eq. (37), and using the Fourier series expansion of $S_{zn'\ell}(v)$ in Eq. (17), it turns out that $Z^{cU3}_{m,n'}$ may be evaluated exactly as

$$Z^{cU3}_{m,n'} = -\pi\left[\frac{\sinh(u_0)}{a}\right]\sum_{i=-I}^{I}\left(a_i^{(m)}(u_0) + a_i^{(-m)}(u_0)\right) S_{z,-i,n',0} \qquad (39)$$

where the Fourier coefficients $a_i^{(m)}(u)$ have been defined earlier in Eq. (27). The final magnetic field equation after evaluating the Kronecker delta function $\delta_{m,m'}$ in Eq. (36) is given by

$$\sum_{n'=1}^{N} Z^{cU3}_{m,n'}U^{SV3}_{hn'} = U^{(3)}_m(r_3^-)\pi[1+\delta_{m,0}] \qquad (40)$$

where the coefficient $U^{SV3}_{hn'}$ has been defined to be $U^{SV3}_{hn'} \equiv U_{hn'\ell}(u')\big|_{u'=0,\rho_3=r_3^+,\ell=0}$ where $U_{hn'\ell}(u')$ is defined in Eq. (24).

A nearly an identical procedure as was used to match EM boundary conditions at the $\rho_3 = r_3$ interface may be used to match EM boundary conditions at the $\rho_1 = r_1,\ u = u_L$ interface. We find that at the $\rho_1 = r_1,\ u = u_L$ interface, that the electric and magnetic field boundary condition equations are given by

$$\sum_{n'=1}^{N} Z^{cE1}_{m,n'}E^{SV1}_{n'} = E^{(1)}_m(r_1^+)\pi[1+\delta_{m,0}] \qquad (41)$$

$$\sum_{n'=1}^{N} Z^{cU1}_{m,n'}U^{SV1}_{hn'} = U^{(1)}_m(r_1^+)\pi[1+\delta_{m,0}] \qquad (42)$$

where

$$E^{SV1}_{n'} \equiv E_{n'\ell}(u')\Big|_{u'=-\Delta u,\rho_1=r_1^-,\ell=L-1} \qquad (43)$$

$$U^{SV1}_{hn'} \equiv U_{hn'\ell}(u')\Big|_{u'=-\Delta u,\rho_1=r_1^-,\ell=L-1} \qquad (44)$$

where the weighting or testing functions $\{\cos(m\phi_1)\},\ m = 0, \ldots, N-1$ have been used to enforce EM boundary conditions over the interval $-\pi \le \phi_1 \le \pi$ in the same way as the $\{\cos(m\phi_3)\},\ m = 0, \ldots, N-1$ were used to enforce boundary conditions at the $\rho_3 = r_3,\ u = u_0$ boundary.

Matching boundary conditions at the $u = u_\ell,\ \ell = 1, 2, \ldots, L-1$ thin layers interfaces (these interfaces are located entirely inside the inhomogeneous region) we have using the electric field expression of Eq. (23) at $u = u_\ell$,

$$E_z^{(2)}(u', u_\ell, v)\Big|_{u'=0} = E_z^{(2)}(u', u_{\ell-1}, v)\Big|_{u'=-\Delta u} \tag{45}$$

or after evaluation, the left hand side of Eq. (45) is

$$E_z^{(2)}(u', u_\ell, v)\Big|_{u'=0} = \sum_{n'=1}^{N} \left\{ C_{n'\ell}^{+} + C_{n'\ell}^{-} \right\} S_{zn'\ell}(v) \equiv \sum_{n'=1}^{N} E_{n'\ell}(0) S_{zn'\ell}(v) \tag{46}$$

the right hand side of Eq. (45) is

$$\begin{aligned} E_z^{(2)}(u', u_{\ell-1}, v)\Big|_{u'=-\Delta u} &= \sum_{n'=1}^{N} \Big\{ C_{n',\ell-1}^{+} \exp(-q_{n',\ell-1}(-\Delta u)) \\ &\quad + C_{n',\ell-1}^{-} \exp(q_{n',\ell-1}(-\Delta u)) \Big\} S_{zn',\ell-1}(v) \\ &\equiv \sum_{n'=1}^{N} E_{n',\ell-1}(-\Delta u) S_{zn',\ell-1}(v) \end{aligned} \tag{47}$$

or altogether

$$\sum_{n'=1}^{N} E_{n'\ell}(0) S_{zn'\ell}(v) = \sum_{n'=1}^{N} E_{n',\ell-1}(-\Delta u) S_{zn',\ell-1}(v) \tag{48}$$

where

$$E_{n',\ell-1}(-\Delta u) = C_{n',\ell-1}^{+} \exp(-q_{n',\ell-1}(-\Delta u)) + C_{n',\ell-1}^{-} \exp(q_{n',\ell-1}(-\Delta u)) \tag{49}$$

$$E_{n'\ell}(0) = C_{n'\ell}^{+} + C_{n'\ell}^{-} \tag{50}$$

To enforce the electric field boundary condition of Eqs. (45), (48), Eq. (48) is multiplied on both sides by the weighting, enforcing, or testing functions $\{S_{zn\ell}(v)\},\ n = 1, 2, \ldots, N$ of Eq. (17), and then integrated over the interval $-\pi \le v \le \pi$. Carrying out this operation and using the property that the functions $\{S_{zn\ell}(v)\}$ are orthonormal (Eq. (18)), it is found that

$$E_{n\ell}(0) = \sum_{n'=1}^{N} E_{n',\ell-1}(-\Delta u) S^{nn'\ell} \tag{51}$$

where

$$S^{nn'\ell} = \int_{-\pi}^{\pi} S_{zn\ell}(v) S_{zn',\ell-1}(v) dv = 2\pi \sum_{i=-I}^{I} S_{zin\ell} S_{z,-i,n',\ell-1} \tag{52}$$

where $\ell = 1, 2, \ldots, L-1$. We note because the eigenfunctions $S_{zn\ell}(v)$ of Eq. (17) change as the value of ℓ changes from interface to interface, that the functions $S_{zn\ell}(v)$ and $S_{zn',\ell-1}(v)$ in the integral of Eq. (52) are not orthogonal, and thus $S^{nn'\ell}$ is nonzero in general when $n \neq n'$.

Evaluating the magnetic field Eq. (24) at $u = u_\ell^\pm$ in a similar way as the electric field was evaluated we find

$$\sum_{n'=1}^{N} U_{hn'\ell}(0) S_{zn'\ell}(v) = \sum_{n'=1}^{N} U_{hn',\ell-1}(-\Delta u) S_{zn',\ell-1}(v) \tag{53}$$

where

$$\begin{aligned} U_{hn'\ell-1}(-\Delta u) &= Z_{n',\ell-1} \left\{ -C_{n',\ell-1}^{+} \exp(-q_{n',\ell-1}(-\Delta u)) \right. \\ &\qquad \left. + C_{n',\ell-1}^{-} \exp(q_{n',\ell-1}(-\Delta u)) \right\} \qquad (54) \\ U_{hn'\ell}(0) &= Z_{n'\ell} \left\{ -C_{n',\ell}^{+} + C_{n',\ell}^{-} \right\} \qquad (55) \end{aligned}$$

If the magnetic field boundary condition of Eq. (53) is multiplied on both sides by the weighting or testing functions $\{S_{zn\ell}(v)\}$ with $n = 1, 2, \ldots, N$ and then integrated over the interval $-\pi \leq v \leq \pi$ it is found, following the same steps as were used done to enforce the electric field boundary condition,

$$U_{hn\ell}(0) = \sum_{n'=1}^{N} U_{hn',\ell-1}(-\Delta u) S^{nn'\ell} \tag{56}$$

where $S^{nn'\ell}$ has been previously defined. By inspecting Eqs. (50) and (55) (after using a value of $\ell - 1$ in these equations) we note that the $C_{n',\ell-1}^{+}$ and $C_{n',\ell-1}^{-}$ coefficients are related to the $E_{n',\ell-1}(0)$ and

$U_{hn',\ell-1}(0)$ coefficients by a simple 2×2 set of equations. If these 2×2 equations are inverted, we find

$$C^{+}_{n',\ell-1} = \left[E_{n',\ell-1}(0) - \frac{1}{Z_{n',\ell-1}}U_{hn',\ell-1}(0)\right]/2 \tag{57}$$

$$C^{-}_{n',\ell-1} = \left[E_{n',\ell-1}(0) + \frac{1}{Z_{n',\ell-1}}U_{hn',\ell-1}(0)\right]/2 \tag{58}$$

If $C^{+}_{n',\ell-1}$ and $C^{-}_{n',\ell-1}$ of Eqs. (57), (58) are substituted back into Eqs. (49) and (54) and the resulting $E_{n',\ell-1}(-\Delta u)$, $U_{hn',\ell-1}(-\Delta u)$, expressions are further substituted back into (51) and (56), we find that the coefficients $E_{n'\ell}(0)$ and $U_{hn'\ell}(0)$ may be expressed in terms of the coefficients $E_{n',\ell-1}(0)$ and $U_{hn',\ell-1}(0)$ by the relations

$$E_{n\ell}(0) = \sum_{n'=1}^{N}\left\{K^{EE}_{nn'\ell}E_{n',\ell-1}(0) + K^{EU}_{nn'\ell}U_{hn',\ell-1}(0)\right\} \tag{59}$$

and

$$U_{n\ell}(0) = \sum_{n'=1}^{N}\left\{K^{UE}_{nn'\ell}E_{n',\ell-1}(0) + K^{UU}_{nn'\ell}U_{hn',\ell-1}(0)\right\} \tag{60}$$

where

$$K^{EE}_{nn'\ell} = K^{UU}_{nn'\ell} = S^{nn'\ell}\cosh[q_{n',\ell-1}(-\Delta u)] \tag{61}$$

$$K^{EU}_{nn'\ell} = \left[S^{nn'\ell}/Z_{n',\ell-1}\right]\sinh[q_{n',\ell-1}(-\Delta u)]$$

$$K^{UE}_{nn'\ell} = \left[S^{nn'\ell}Z_{n',\ell-1}\right]\sinh[q_{n',\ell-1}(-\Delta u)] \tag{62}$$

where $\ell = 1, 2, \ldots, L-1$ and where $\cosh(\cdot)$ and $\sinh(\cdot)$ represent the hyperbolic cosine and hyperbolic sine functions respectively. Defining the $N\times N$ matrices $\underline{\underline{K^{EE}_{\ell}}} \equiv \left[K^{EE}_{nn'\ell}\right]$, $\underline{\underline{K^{EU}_{\ell}}} \equiv \left[K^{EU}_{nn'\ell}\right]$, $\underline{\underline{K^{UE}_{\ell}}} \equiv \left[K^{UE}_{nn'\ell}\right]$ and $\underline{\underline{K^{UU}_{\ell}}} \equiv \left[K^{UU}_{nn'\ell}\right]$ with $(n, n') = 1, 2, \ldots, N$, defining the column matrices $\underline{E_{\ell}} \equiv [E_{n\ell}(0)]$ and $\underline{U_{h\ell}} \equiv [U_{hn\ell}(0)]$ with $n = 1, 2, \ldots, N$, defining the $2N \times 2N$ matrix

$$\underline{\underline{K_{\ell}}} \equiv \begin{bmatrix} \underline{\underline{K^{EE}_{\ell}}} & \underline{\underline{K^{EU}_{\ell}}} \\ \underline{\underline{K^{UE}_{\ell}}} & \underline{\underline{K^{UU}_{\ell}}} \end{bmatrix} \tag{63}$$

and the $2N$ column matrix

$$\underline{W_{\ell}} \equiv \begin{bmatrix} \underline{E_{\ell}} \\ \underline{U_{h\ell}} \end{bmatrix} \tag{64}$$

we find

$$\begin{bmatrix} \underline{E_\ell} \\ \underline{U_{h\ell}} \end{bmatrix} \equiv \begin{bmatrix} \underline{\underline{K_\ell^{EE}}} & \underline{\underline{K_\ell^{EU}}} \\ \underline{\underline{K_\ell^{UE}}} & \underline{\underline{K_\ell^{UU}}} \end{bmatrix} \begin{bmatrix} \underline{E_{\ell-1}} \\ \underline{U_{h\ell-1}} \end{bmatrix} \tag{65}$$

or

$$\underline{W_\ell} = \underline{\underline{K_\ell}}\,\underline{W_{\ell-1}} \tag{66}$$

where $\ell = 1, \ldots, L-1$. We thus see that the electric and magnetic field coefficients $E_{n\ell}(0)$ and $U_{hn\ell}(0)$, $n = 1, \ldots, N$ of the eigenfunctions $S_{zn\ell}(v)$ which corresponds to the $u = u_\ell$ layer, may be expressed in terms of the electric and magnetic field coefficients $E_{n,\ell-1}(0)$ and $U_{hn,\ell-1}(0)$ of the eigenfunctions $S_{zn,\ell-1}(v)$ at $u = u_{\ell-1}$ layer. By starting at $\ell = 1$ and by successive substitution, it is found that

$$\underline{W_{L-1}} = \underline{\underline{K_{L-1}}}\,\underline{\underline{K_{L-2}}} \ldots \underline{\underline{K_2}}\,\underline{\underline{K_1}}\,\underline{W_0} \tag{67}$$

Forming the column matrices $\underline{E^{SV1}} = [E_n^{SV1}]$, $\underline{U_h^{SV1}} = [U_{hn}^{SV1}]$, $n = 1, \ldots, N$, where E_n^{SV1} and U_{hn}^{SV1} are defined by Eqs. (43), (44), we further find that the electric and magnetic field coefficients $E_{n,L-1}(0)$ and $U_{hn,L-1}(0)$ of $u = u_{L-1}$ the interface are related to the field coefficients E_n^{SV1} and U_{hn}^{SV1} of the $u = u_L$, $\rho_1 = r_1$ interface, after using $\ell = L$ in Eqs. (61)–(63), by the matrix relation

$$\underline{W_L} \equiv \begin{bmatrix} \underline{E^{SV1}} \\ \underline{U_h^{SV1}} \end{bmatrix} = \begin{bmatrix} \underline{\underline{K_L^{EE}}} & \underline{\underline{K_L^{EU}}} \\ \underline{\underline{K_L^{UE}}} & \underline{\underline{K_L^{UU}}} \end{bmatrix} \begin{bmatrix} \underline{E_{L-1}} \\ \underline{U_{h,L-1}} \end{bmatrix} \equiv \underline{\underline{K_L}}\,\underline{W_{L-1}} \tag{68}$$

We further note that at the $\ell = 0$ interface, after letting $\underline{W_0} \equiv \begin{bmatrix} \underline{E^{SV3}} \\ \underline{U_h^{SV3}} \end{bmatrix}$ where $\underline{E^{SV3}} \equiv [E_n^{SV3}]$ and $\underline{U_h^{SV3}} \equiv [U_{hn}^{SV3}]$, $n = 1, \ldots, N$, where E_n^{SV3} and U_{hn}^{SV3} are defined by Eqs. (35) and (40) respectively, that

$$\underline{W_L} = \underline{\underline{K_L}}\,\underline{\underline{K_{L-1}}} \ldots \underline{\underline{K_2}}\,\underline{\underline{K_1}}\,\underline{W_0} \equiv \underline{\underline{K}}\,\underline{W_0} \tag{69}$$

We thus see that matrix $\underline{\underline{K}}$ relates the SV coefficients of the inner layer to the SV coefficients outer one.

Our objective now as mentioned in the Introduction is to develop from the SV solution a transfer matrix which relates the circular Bessel-Fourier coefficients of $\cos(m\phi_3)$, $m = 0, N-1$ associated with the electric and magnetic fields on the inner cylinder $\rho_3 = r_3^-$ to the circular Bessel-Fourier coefficients of $\cos(m\phi_1)$, $m = 0, N-1$, associated with the electric and magnetic fields the outer cylinder $\rho_1 = r_1^+$. These may be accomplished by; (1) expressing the coefficients $E_m^{(1)}(r_1^+)$, $U_m^{(1)}(r_1^+)$, in terms of SV coefficients E_n^{SV1}, U_{hn}^{SV1} by Eqs. (41), (42); (2) expressing the SV coefficients E_n^{SV1}, U_{hn}^{SV1}, in terms of E_n^{SV3}, U_{hn}^{SV3}, by using the matrix $\underline{\underline{K}}$ of Eq. (69); (3) expressing the SV coefficients E_n^{SV3}, U_{hn}^{SV3}, in terms of the coefficients $E_m^{(3)}(r_3^-)$, $U_m^{(3)}(r_3^-)$, through Eqs. (28), (29) and; (4) substituting successively the coefficient relations mentioned in Steps (1–3) to finally express $E_m^{(1)}(r_1^+)$, $U_m^{(1)}(r_1^+)$, in terms of $E_m^{(3)}(r_3^-)$, $U_m^{(3)}(r_3^-)$.

The SV coefficients E_n^{SV3}, U_{hn}^{SV3}, may be found in terms $E_m^{(3)}(r_3^-)$, $U_m^{(3)}(r_3^-)$, respectively, by multiplying Eq. (28) by $S_{zn\ell}(v)$, $\ell = 0$, by multiplying Eq. (29) by $-h(u_0, v)S_{zn\ell}(v)$, $\ell = 0$, and then integrating the resulting equations over the range $-\pi \le v \le \pi$. Performing these operations after using the orthonormal property of the $S_{zn\ell}(v)$, $n = 1, \ldots, N$, $\ell = 0$ eigenfunctions it is found

$$\begin{aligned} E_n^{SV3} &\equiv E_{n\ell}(u')\Big|_{u'=0,u=u_0,\ell=0} \\ &= \sum_{m=0}^{N-1} E_m^{(3)}(r_3^-)\left[\int_{-\pi}^{\pi} S_{zn0}(v)\cos(m\phi_3(v))dv\right] \end{aligned} \tag{70}$$

$$\begin{aligned} U_{hn}^{SV3} &\equiv U_{hn\ell}(u')\Big|_{u'=0,u=u_0,\ell=0} \\ &= \sum_{m=0}^{N-1} U_m^{(3)}(r_3^-)\left[-\int_{-\pi}^{\pi} S_{zn0}(v)h(u_0, v)\cos(m\phi_3(v))dv\right] \end{aligned} \tag{71}$$

If one expands $S_{zn0}(v)$ and the exponentials $\exp(\pm jm\phi_3(v))$ which make up $\cos(m\phi_3(v))$ in an the exponential Fourier series in the variable v given by Eq. (27), one finds after substituting the Fourier series of the two terms and using the orthogonality of the Fourier exponentials $\exp(jiv)$, $i = -I, \ldots, I$, that the integral in Eq. (70) is given by

$$\begin{gathered} E_n^{SV3} \equiv \sum_{m=0}^{N-1} Z_{nm}^{SE3} E_m^{(3)}(r_3^-), \\ Z_{nm}^{SE3} = \pi \sum_{i=-I}^{I} \left[\alpha_{-i}^{(m)}(u_0) + \alpha_{-i}^{(-m)}(u_0)\right] S_{zin0} \end{gathered} \tag{72}$$

The integral in Eq. (71) may be evaluated by; (1) expanding the cosine exponential factors $\exp(jp\phi_3(v))/(\cosh(u_0) - \cos(v)) = \exp(jp\phi_3(v))(h(u_0, v)/a)$, $p = \pm m$ which occur in this integral as an exponential Fourier series

$$\exp(jp\phi_3(v))/(\cosh(u_0)-\cos(v)) = \sum_{i=-\infty}^{\infty} \beta_i^{(p)}(u_0)\exp(jiv) \tag{73}$$

(details given in Appendix A); (2) substituting the $\exp(jiv)$ Fourier expansion for $S_{zn0}(v)$ of Eq. (17); and (3) carrying out the resulting integral over $-\pi \le v \le \pi$ with respect to v and using the orthogonality of the $\exp(jiv)$ exponentials. From these steps it is found

$$\begin{aligned} U_{hn}^{SV3} &\equiv \sum_{m=0}^{N-1} Z_{nm}^{SU3} U_m^{(3)}(r_3^-), \\ Z_{nm}^{SU3} &= -\pi a \sum_{i=-I}^{I} \left[\beta_{-i}^{(m)}(u_0) + \beta_{-i}^{(-m)}(u_0)\right] S_{zin0} \end{aligned} \tag{74}$$

If Eqs. (72), (74) are put in matrix form with $\underline{\underline{Z^{SE3}}} = [Z_{nm}^{SE3}]$, $\underline{\underline{Z^{SU3}}} = [Z_{nm}^{SU3}]$, $\underline{E^{(3)}} = [E_m^{(3)}(r_3^-)]$, $\underline{U^{(3)}} = [U_m^{(3)}(r_3^-)]$ with $m = 0,\ldots,N-1$, and $n = 1,\ldots,N$, we have (Eq. (69))

$$\underline{W_0} \equiv \begin{bmatrix} \underline{E^{SV3}} \\ \underline{U_h^{SV3}} \end{bmatrix} = \begin{bmatrix} \underline{\underline{Z^{SE3}}} & 0 \\ 0 & \underline{\underline{Z^{SU3}}} \end{bmatrix} \begin{bmatrix} \underline{E^{(3)}} \\ \underline{U^{(3)}} \end{bmatrix} \equiv \underline{\underline{Z^{(3)}}}\,\underline{W^{(3)}} \tag{75}$$

The coefficients $E_m^{(1)}(r_1^+)$, $U_m^{(1)}(r_1^+)$ are given by, after using Eqs. (41), (42)

$$E_m^{(1)}(r_1^+) = \sum_{n=1}^{N} Z_{mn}^{CE1} E_n^{SV1}, \quad Z_{mn}^{CE1} \equiv \frac{1}{\pi(1+\delta_{m,0})} Z_{mn}^{cE1} \tag{76}$$

$$U_m^{(1)}(r_1^+) = \sum_{n=1}^{N} Z_{mn}^{CU1} U_{hn}^{SV1}, \quad Z_{mn}^{CU1} \equiv \frac{1}{\pi(1+\delta_{m,0})} Z_{mn}^{cU1} \tag{77}$$

If Eqs. (76), (77) are put in matrix form with $\underline{\underline{Z^{CE1}}} = [Z_{mn}^{CE1}]$, $\underline{\underline{Z^{CU1}}} = [Z_{mn}^{CU1}]$, $\underline{E^{(1)}} = [E_m^{(1)}(r_1^+)]$, $\underline{U^{(1)}} = [U_m^{(1)}(r_1^+)]$ with $m = 0,\ldots,N-1$ and $n = 1,\ldots,N$ we have

$$\begin{bmatrix} \underline{E^{(1)}} \\ \underline{U^{(1)}} \end{bmatrix} = \begin{bmatrix} \underline{\underline{Z^{CE1}}} & 0 \\ 0 & \underline{\underline{Z^{CU1}}} \end{bmatrix} \begin{bmatrix} \underline{E^{SV1}} \\ \underline{U_h^{SV1}} \end{bmatrix} \equiv \underline{\underline{Z^{(1)}}} \begin{bmatrix} \underline{E^{SV1}} \\ \underline{U_h^{SV1}} \end{bmatrix} \tag{78}$$

Letting $\underline{W^{(1)}} \equiv \begin{bmatrix} \underline{E^{(1)}} \\ \underline{U^{(1)}} \end{bmatrix}$, using $\underline{W_L} \equiv \begin{bmatrix} \underline{E^{SV1}} \\ \underline{U_h^{SV1}} \end{bmatrix}$ which is defined in Eq. (68), we have altogether $\underline{W^{(1)}} = \underline{\underline{Z^{(1)}}}\,\underline{W_L}$, $\underline{W_L} = \underline{\underline{K}}\,\underline{W_0}$, from

Eq. (69), and $\underline{W_0} = \underline{\underline{Z^{(3)}}}\,\underline{W^{(3)}}$ from Eq. (75), or after substitution, $\underline{W^{(1)}} = \underline{\underline{Z^{(1)}}}\,\underline{\underline{K}}\,\underline{\underline{Z^{(3)}}}\,\underline{W^{(3)}}$. We have

$$\begin{aligned}\begin{bmatrix} \underline{E^{(1)}} \\ \underline{U^{(1)}} \end{bmatrix} &= \begin{bmatrix} \underline{\underline{K^{SVEE}_{r_1;r_3}}} & \underline{\underline{K^{SVEU}_{r_1;r_3}}} \\ \underline{\underline{K^{SVUE}_{r_1;r_3}}} & \underline{\underline{K^{SVUU}_{r_1;r_3}}} \end{bmatrix} \begin{bmatrix} \underline{E^{(3)}} \\ \underline{U^{(3)}} \end{bmatrix} = \underline{\underline{K^{SV}_{r_1;r_3}}} \begin{bmatrix} \underline{E^{(3)}} \\ \underline{U^{(3)}} \end{bmatrix} \\ &= \underline{\underline{Z^{(1)}}}\,\underline{\underline{K}}\,\underline{\underline{Z^{(3)}}} \begin{bmatrix} \underline{E^{(3)}} \\ \underline{U^{(3)}} \end{bmatrix} \end{aligned} \tag{79}$$

where we have defined $\underline{\underline{K^{SV}_{r_1;r_3}}} \equiv \underline{\underline{Z^{(1)}}}\,\underline{\underline{K}}\,\underline{\underline{Z^{(3)}}}$. This relation thus uses state variable techniques to express, respectively, the electric and magnetic field coefficients $E^{(1)}_m(r_1^+)$, $U^{(1)}_m(r_1^+)$ of $\cos(m\phi_1)$ in terms of the electric and magnetic field coefficients $E^{(3)}_m(r_3^-)$, $U^{(3)}_m(r_3^-)$ of $\cos(m\phi_3)$. The matrix $\underline{\underline{K^{SV}_{r_1;r_3}}}$, which may be called a transfer matrix since it relates or transfers the electric and magnetic field Fourier coefficients from the Reg. 3 inner boundary to the electric and magnetic field Fourier coefficients of the Reg. 1 exterior interface, is useful for defining an overall matrix from which all unknowns of the system may be found.

The transfer matrix of Eq. (79) is also useful because in the case when uniform materials occupy the regions between the interfaces of adjacent, eccentric cylinders, it may be compared directly to the exact, Bessel function addition theorem analysis that was developed by KPE [22] after an algebraic manipulation of the form of the KPE algorithm is made. This is very useful because by comparing the matrix elements of the SV transfer matrix $\underline{\underline{K^{SV}_{r_1;r_3}}}$ and the matrix elements of the Bessel function transfer matrix, call it $\underline{\underline{K^{B}_{r_1;r_3}}}$, based on the KPE method [22], one can gain insight into how well the SV method is converging with respect to the number of modes used, the number of layers, the Fourier matrix truncation size, etc.. Appendix B specifies and gives a derivation of the Bessel function transfer matrix $\underline{\underline{K^{B}_{r_1;r_2}}}$ that results from the KPE algorithm [22] for a single layer between two adjacent interfaces containing a uniform material and Appendix B also presents the theory of how to cascade together single layer, uniform material, Bessel, transfer matrices to form the overall transfer matrix of a multiple, eccentric cylinder system. For example, for the two layer, three interface composite cylinder shown in Fig. 2, the cascaded Bessel transfer matrix $\underline{\underline{K^{B}_{r_1;r_3}}}$ would be given by $\underline{\underline{K^{B}_{r_1;r_3}}} = \underline{\underline{K^{B}_{r_1;r_2}}}\,\underline{\underline{K^{B}_{r_2;r_3}}}$ where $\underline{\underline{K^{B}_{r_1;r_2}}}$ and $\underline{\underline{K^{B}_{r_2;r_3}}}$ are single layer transfer matrices.

As a numerical example of a comparison the SV and Bessel transfer matrices we again consider the scattering object shown in Fig. 2 and we consider the numerical case when the SV matrix was determined using $L = 4200$ layers and $N = 30$ modes. It was found numerically that for $m = 4,\ m' = 8$ the SV and Bessel transfer EE submatrix elements had respectively the values;

$$\begin{aligned} \underline{\underline{K_{r_1;r_3}^{SVEE}}}(4,8) &= 8.0877 \times 10^{-3} \\ \underline{\underline{K_{r_1;r_3}^{BEE}}}(4,8) &= 8.0901 \times 10^{-3} \end{aligned}$$

and the state variable and Bessel transfer UE submatrix elements had respectively the values;

$$\begin{aligned} \underline{\underline{K_{r_1;r_3}^{SVUE}}}(4,8) &= -j2.4427 \times 10^{-2} \\ \underline{\underline{K_{r_1;r_3}^{BUE}}}(4,8) &= -j2.4533 \times 10^{-2} \end{aligned}$$

The data shown represents relatively good agreement between the methods.

So far the state variable transfer matrix has been derived to express the electric and magnetic field coefficient column matrix evaluated at $\rho_1 = r_1$ in terms of electric and magnetic field coefficient column matrix evaluated at $\rho_3 = r_3$. We would like to mention at this point that the state variable transfer matrix, call it $\underline{\underline{K_{r_u;r_3}^{SV}}}$, which expresses the electric and magnetic field coefficient column matrix evaluated at an intermediate layer in the inhomgeneous region, say $\rho_u = r_u,\ u = u_\ell$, in terms of electric and magnetic field coefficient column matrix evaluated at $\rho_3 = r_3$, may be defined by simply cascade multiplying the matrices of Eq. (69) through all layers between $\rho_3 = r_3$ and the intermediate layer $\rho_u = r_u,\ u = u_\ell$, call this matrix $\underline{\underline{K_{u_\ell;u_0}}}$, and then forming $\underline{\underline{K_{r_u;r_3}^{SV}}} = \underline{\underline{Z^{(u)}}}\,\underline{\underline{K_{u_\ell;u_0}}}\,\underline{\underline{Z^{(3)}}}$ where $\underline{\underline{Z^{(u)}}}$ is defined at the intermediate layer $\rho_u = r_u,\ u = u_\ell$, rather than at $\rho_1 = r_1$ as was $\underline{\underline{Z^{(1)}}}$ of Eq. (78). The transfer matrix $\underline{\underline{K_{r_u;r_3}^{SV}}}$ is very helpful for post processing because it may be used to find the cylindrical Fourier, electric and magnetic coefficients $E_m(r_u)$, $U_m(r_u)$, of $\cos(m\phi_u)$, $m = 0,\ldots,N-1$, at any desired internal layer interface $\rho_u = r_u,\ u = u_\ell$, once the coefficients $E_m^{(3)}(r_3^-)$, $U_m^{(3)}(r_3^-)$ are found. All calculations of the EM fields inside the inhomogeneous region of the scattering object were made in this paper by finding the coefficients $E_m(r_u)$, $U_m(r_u)$, at all intermediate interfaces using the intermediate transfer matrix $\underline{\underline{K_{r_u;r_3}^{SV}}}$ and then summing the appropriate Fourier cosine series.

We now are in a position to define an overall system matrix from which all unknowns of the system may be determined. We will use the SV transfer matrix of Eq. (79). At $\rho_3 = r_3^-$ the electric and magnetic field Fourier coefficients from Eqs. (19), (20) are given by $m = 0, 1, \ldots, N-1$

$$E_m^{(3)}(r_3^-) = A_m^{(3)} J_m(k_3 r_3^-) + B_m^I H_m^{(2)}(k_3 r_3^-) \tag{80}$$

$$U_m^{(3)}(r_3^-) = \left[\frac{k_3}{j\mu_3}\right] \left[A_m^{(3)} J_m'(k_3 r_3^-) + B_m^I H_m^{(2)'}(k_3 r_3^-)\right] \tag{81}$$

If the $A_m^{(3)}$ coefficients of Eq. (80) is substituted into Eq. (81), it turns out that

$$\frac{J_m'(k_3 r_3^-)}{J_m(k_3 r_3^-)} E_m^{(3)}(r_3^-) - \frac{j\mu_3}{k_3} U_m^{(3)}(r_3^-) = \frac{2jB_m^I}{(\pi k_3 r_3^-) J_m(k_3 r_3^-)} \tag{82}$$

In deriving Eq. (82) the Wronskian relation $J_m'(X) H_m^{(2)}(X) - J_m(X) H_m^{(2)'}(X) = \frac{2j}{\pi X}$ was used. (Use of the Wronskian eliminated the Hankel function and its derivative from Eq. (82)). At the $\rho_1 = r_1^+$ a similar analysis as was performed at $\rho_3 = r_3^-$, shows for $m = 0, 1, \ldots, N-1$

$$\frac{H_m^{(2)'}(k_0 r_1^+)}{H_m^{(2)}(k_0 r_1^+)} E_m^{(1)}(r_1^+) - \frac{j\mu_0}{k_0} U_m^{(1)}(r_1^+) = \frac{-2jA_m^I \cos(m\phi_0)}{(\pi k_0 r_1^+) H_m^{(2)}(k_0 r_1^+)} \tag{83}$$

In this paper it is assumed that there are no internal sources in Reg. 3, thus $B_m^I = 0$, and that a plane wave of amplitude $E_0^P = 1.0$ (Volt/m) is incident of the scattering object (see Fig. 2) and thus $A_m^I = E_0^P (2 - \delta_{m,0}) j^m$. Eqs. (82), (83), along with the transfer matrix of Eq. (79), form an overall $4N \times 4N$ system matrix system from which the unknowns, namely $E_m^{(3)}(r_3^-)$, $U_m^{(3)}(r_3^-)$, $E_m^{(1)}(r_1^+)$, $U_m^{(1)}(r_1^+)$, $m = 0, 1, \ldots, N-1$, may be determined. Once these unknowns are found all other unknowns of the system may be determined.

As mentioned earlier, the SV transfer matrix of Eq. (79) has been derived to express the $\rho_1 = r_1$ (or $u = u_L$) electric and magnetic field column matrices in terms of the $\rho_3 = r_3$ (or $u = u_0$) electric and magnetic field column matrices. This may be referred to as an outward transfer matrix as one starts at the inner boundary $\rho_3 = r_3$ and cascade multiplies the layer to layer matrices $\underline{\underline{K_\ell}}$ in Eq. (69) in an outward direction from $\rho_3 = r_3$ to $\rho_1 = r_1$. We would like to note at this point that the formulation that has been presented in Eqs. (45)–(79) can also be used to derive a transfer matrix which does the reverse of what the present transfer matrix $\underline{\underline{K}}^{SV}_{r_1;r_3}$ does, namely express the $\rho_3 = r_3$ electric and magnetic field column matrices in terms of the $\rho_1 = r_1$ electric and magnetic field column matrices. This may be accomplished by simply using Δu ($\Delta u > 0$) in Eqs. (45)–(79) rather than ($-\Delta u$) as was used, and then cascade multiplying the resulting equations in an inward direction from $\rho_1 = r_1,\ u = u_L$, to $\rho_3 = r_3,\ u = u_0$, rather than the outward direction. The resulting transfer matrix $\underline{\underline{K}}^{SV}_{r_3;r_1}$ may be called an inward transfer matrix as it is formed by cascade multiplying the resulting equations in an inward direction from $\rho_1 = r_1,\ u = u_L$, to $\rho_3 = r_3,\ u = u_0$. If the inward transfer matrix $\underline{\underline{K}}^{SV}_{r_3;r_1}$ is used to formulate the overall system matrix equations, one then forms a different overall system matrix than is formed by using the outward $\underline{\underline{K}}^{SV}_{r_1;r_3}$ transfer matrix. In addition to overall system matrix formulations based on pure outward or inward transfer matrices, one may also develop a mixed overall system matrix formulation where one uses a combination of an inward and outward transfer matrices. In this mixed formulation, with the use of the outward and inward transfer matrices, EM boundary conditions are enforced at an interface inside the inhomogeneous scattering object. The ability to develop overall system matrices based on outward, inward, or mixed sets of transfer matrices is very useful as it allows one to implement different overall system matrices, which thus provides a method to at least partially cross check numerical results by comparing the numerical results of the different, overall system matrix solutions. Numerical testing has shown that in all cases tested, that the pure outward transfer matrix produced the most accurate results when compared to the KPE algorithm [22], but that acceptable numerical solutions were also found using the mixed and backward transfer matrix solutions.

Once the EM fields of the system are known an important scattering quantity to determine is the bistatic scattering width per unit wavelength (the wavelength is taken in the medium which the scattering object is located (free space in this paper)). The scattering width (also called radar cross section per unit length) in units of *meters* is defined by [25]

$$\sigma_{2-D}(\phi,\phi_0) = \lim_{\tilde{\rho}_1\to\infty} 2\pi\tilde{\rho}_1 \frac{|E_z^s|^2}{|E_z^{INC}|^2}, \tag{84}$$

thus bistatic scattering width per unit wavelength is defined by

$$\sigma(\phi,\phi_0) \equiv \frac{\sigma_{2-D}(\phi,\phi_0)}{\tilde{\lambda}_0} \tag{85}$$

where here we take $\tilde{\lambda}_0 = 1$ meter. In Eq. (84) E_z^{INC} is the incident plane wave of the system assumed to have an amplitude value $E_0^P = 1.0$ (Volt/m), ϕ is the scattering angle (measured from the X_1 axis of Figs. 1 and 2), ϕ_0 is the angle of incidence of the plane wave and E_z^s is the scattered electric field of the system. When E_z^s is substituted in Eq. (84) it is found, after the symmetry of the present scattering case is taken into account that

$$E_z^s = \sum_{m=0}^{\infty} B_m^{(0)} H_m^{(2)}(\tilde{k}_0 \tilde{\rho}_1) \cos(m\phi_0) \cos(m\phi) \tag{86}$$

When the Hankel functions $H_m^{(2)}(\tilde{k}_0 \tilde{\rho}_1)$ which make up the E_z^s scattered fields are expanded asymmptotically as $\tilde{\rho}_1 \to \infty$, it is found

$$\sigma(\phi, \phi_0) = \frac{2}{\pi} |F^s(\phi, \phi_0)|^2 \tag{87}$$

where

$$F^s(\phi, \phi_0) = \sum_{m=0}^{\infty} j^m B_m^{(0)} \cos(m\phi_0) \cos(m\phi) \tag{88}$$

Eq. (87) is the scattering cross section equation used by KPE [22, Eq. (19)]. (Please keep in mind that KPE [22] studied scattering from composite cylinders which were not in general symmetric, so that $F^s(\phi, \phi_0)$ given in [22] was expressed as an exponential series from $m = -\infty, \ldots, \infty$ rather than the cosine series given in Eq. (88).)

We would like to mention that an important aspect of the RCWA algorithm that is being developed herein is to properly validate the numerical results of the algorithm. In this paper this may be accomplished in the following ways. The first way is to compare numerical results from the RCWA algorithm with the numerical results KPE algorithm as presented in [22] for cases for which the KPE applies, namely multiple eccentric cylinders containing uniform materials between the cylinder interfaces. To accomplish this the author of this paper has programmed the KPE algorithm as presented in [22], has programmed the exact matrix equations presented in [22], and except for a minor computational change (which was to invert layer to layer matrices of [22] to obtain a reduced system matrix as opposed to solving a large system as was done in [22]), the exact KPE algorithm was used to compute comparison validation results. A second way to validate the RCWA method is to use the Bessel, cascaded, transfer matrix, $\underline{\underline{K_{r_1;r_3}^{B}}}$ (which is based on the KPE algorithm) which was derived in Appendix B to formulate the overall matrix of the system rather than use the outward SV transfer matrix $\underline{\underline{K_{r_1;r_3}^{SV}}}$. Numerical

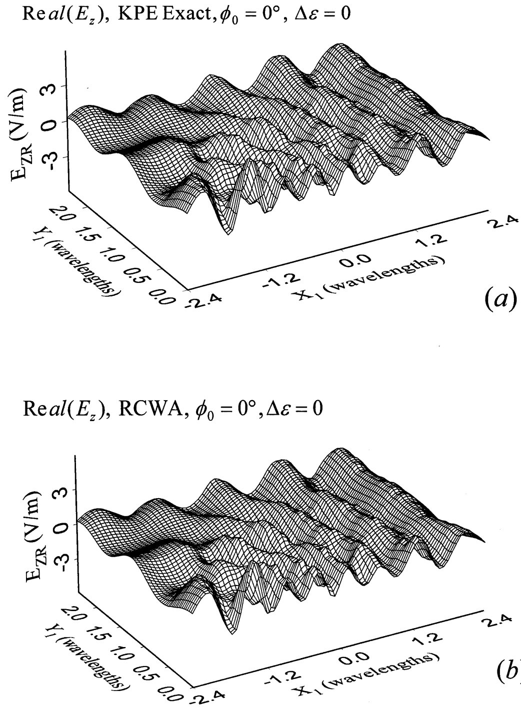

Figure 4. Figs. a and b show, respectively, for the scattering model described in Figs. 1, 2, 3a and Sec. 3 for $\phi_0 = 0°$, the real part of the electric field E_z, E_{zR}, that results when the KPE method [22] is used to calculate E_{zR} (Fig. a) and when the RCWA method was used to calculate E_{zR} (Fig. b).

calculations for several different examples showed that both the original KPE algorithm as presented in [22] and the KPE algorithm based on the Bessel transfer matrix $\underline{\underline{K_{r_1;r_3}^B}}$, gave virtually identical results. A third way of validating results when the KPE or Bessel transfer matrix formulation didn't apply (i.e., spatially non uniform materials between the cylinder interfaces), was to compare matrix results using the outward SV transfer matrix formulation with matrix results using a mixed, outward-inward transfer matrix formulation. In the next section many validation results are presented. We mention that for validation cases involving the KPE algorithm to be presented, that only the KPE algorithm as originally presented in [22] (referred as the first way) was used, as this seemed to be the most independent way to compare numerical results of the two algorithms.

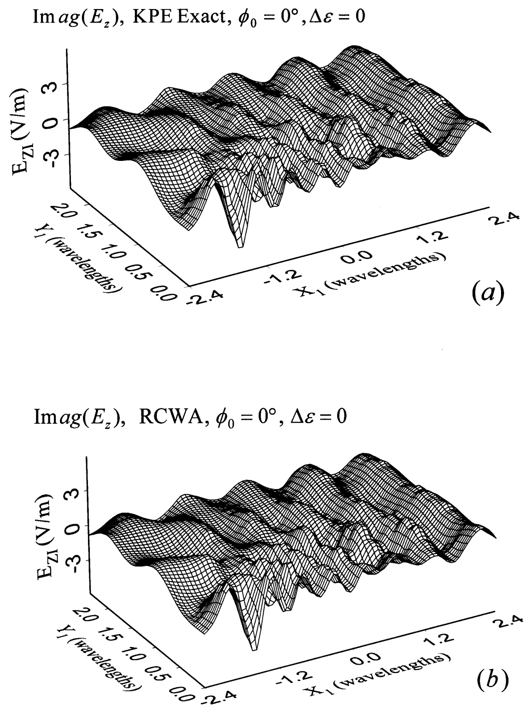

Figure 5. Figs. a and b show for the same case described in Fig. 4, the imaginary part of the electric field E_z, E_{zI}, that results when the KPE method [22] is used to calculate E_{zI} (Fig. a) and when the RCWA method was used to calculate E_{zI} (Fig. b).

3. NUMERICAL RESULTS

This section will present several numerical examples of the theory in Sec. 2. As mentioned in the previous section the author of the present paper has programmed the KPE algorithm as presented in [22] and has used this algorithm to validate all examples which may be analyzed using the KPE algorithm. In the following examples the permeability is assumed to be that of free space everywhere. For all computations in this paper the spectral domain truncation index I was taken to have a value $I = N + 2$ or $I = N + 3$ where N was the number of modes used in RCWA calculation.

As a first example, we refer to KPE [22], Fig. 6, middle curve (TM case, $E_z \neq 0$) which displays the backscatter width $\sigma_b \equiv \sigma(\phi_0, \phi_0)$ as a function of the angle incidence ϕ_0. For this example, the scattering

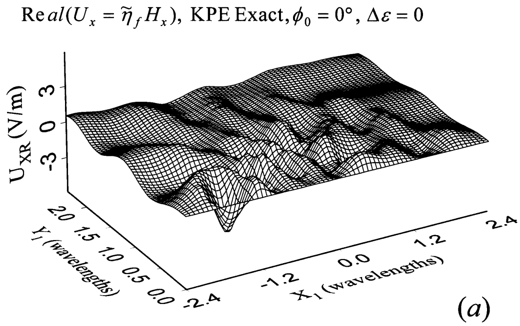

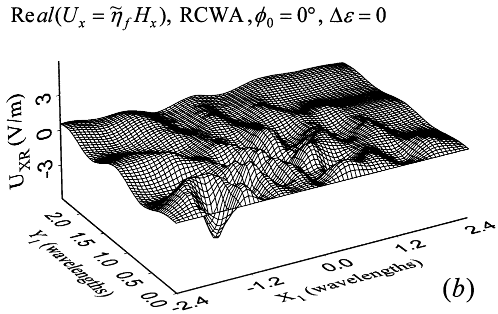

Figure 6. Figs. a and b show for the same case described in Fig. 4, the real part of the magnetic field $U_x = \tilde{\eta}_f H_x$, U_{xR}, that results when the KPE method [22] is used to calculate U_{xR} (Fig. a) and when the RCWA method was used to calculate U_{xR} (Fig. b).

object consists of a one layer eccentric circular cylinder where the inner radius is $\tilde{r}_2 = 0.3183\tilde{\lambda}_f$, where the outer radius $\tilde{r}_1 = 2\tilde{r}_2$, and where the inner cylinder center is displaced a distance $\tilde{e}_{12} = 0.1\tilde{\lambda}_f$ to the right of the center of the outer cylinder. The relative permittivity; of the inner cylinder is $\varepsilon_2 = 4.0$, of the layer between the inner and outer cylinders is $\varepsilon_1 = 2.0$; and of the region exterior to the outer cylinder is $\varepsilon_0 = 1.0$. Two data points in Fig. 6 [22] that can be compared directly to the present symmetry case under analysis in this paper, correspond to the Fig. 6 [22] data points when the angle of incidence is 0° and when it is 180°. When the angle of incidence in KPE [22] Fig. 6 was 0°, the KPE algorithm written by the author of this paper calculated numerically a backscatter width value of $\sigma_b^{\text{KPE}} = 0.21628129000863$, whereas the RCWA method for the same orientation of the plane wave to the scattering object as was used in [22], gave a value of

$\sigma_b^{\text{RCWA}} = 0.21628129000806$. Direct visual inspection of the KPE Fig. 6 graph [22] showed a value approximately of $\sigma_b^{\text{KPE}} \cong 0.22$ for this case. When the angle of incidence in KPE [22] Fig. 6 was 180°, the KPE algorithm written by the author of this paper calculated numerically a backscatter width value of $\sigma_b^{\text{KPE}} = 2.62566962481638$ whereas the RCWA method for the same orientation of the plane wave to the scattering object gave a value of $\sigma_b^{\text{RCWA}} = 2.62566962481619$. Direct visual inspection of the KPE Fig. 6 graph [22] showed a backscatter width value approximately of $\sigma_b^{\text{KPE}} \cong 2.63$. Extremely close agreement for this example is seen between the KPE and RCWA methods.

The second example to be presented corresponds to the two layer, three interface, eccentric cylinder system shown in Fig. 2. Recalling the original definitions $\rho_j \equiv \tilde{k}_f \tilde{\rho}_j,\ r_j \equiv \tilde{k}_f \tilde{r}_j,\ R_j \equiv r_j/2\pi,\ j = 1, 2, 3$ where $\tilde{k}_f \equiv 2\pi/\tilde{\lambda}_f$, where $\tilde{\rho}_j, \tilde{r}_j$ are in units of meters, Fig. 1 shows dimensions and coordinates of the interior region ($u > u_0,\ \rho_3 < r_3$), the inhomogeneous region ($u_L \leq u \leq u_0$), and the exterior region ($u < u_L,\ \rho_1 > r_1$), whereas Fig. 2 shows the geometry of relative dielectric material inhomogeneity $\varepsilon(u, v)$. In this example the inner cylinder is defined by a radius of $\tilde{r}_3 = 1.0\tilde{\lambda}_f$ and its center is displaced a distance $\tilde{e}_{13} = 0.31415926\tilde{\lambda}_f$ to the left of the outer cylinder center; the outer cylinder is defined by a radius of $\tilde{r}_1 = 2.0\tilde{\lambda}_f$; and the cylinder circumscribed between the inner and outer cylinders as shown in Fig. 2, is an intermediate cylinder of radius $\tilde{r}_2 = 1.34292036\tilde{\lambda}_f$ which is offset a distance $\tilde{e}_{12} = 0.65770796\tilde{\lambda}_f$ to the left of the outer cylinder center. The bipolar parameter had a value of $a = \tilde{k}_f \tilde{a} = 28.32451318$ for the system shown in Figs. 1 and 2. As can be seen from Fig. 2, the intermediate cylinder contains the inner cylinder, and the intermediate cylinder is contained by the outer cylinder. For this example the inhomogeneity profile which will be studied (see Fig. 2) is given by

$$\varepsilon(u, v) = \begin{cases} \varepsilon_1 + \Delta\varepsilon \cos(\Lambda u) \cos(\alpha v), & \text{when } (u, v) \text{ is in Reg. 1} \\ \varepsilon_2, & \text{when } (u, v) \text{ is in Reg. 2} \end{cases} \tag{89}$$

where Reg. 1 is the region bounded by $\rho_1 = r_1$ on the outside and $\rho_2 = r_2$ on the inside and where Reg. 2 is the region bounded by $\rho_2 = r_2$ on the outside and $\rho_3 = r_3$ on the inside. Figs. 3a, 3b, and 3c show respectively, plots of $\varepsilon(X_1, Y_1)$ (found from $\varepsilon(u, v)$ of Eq. (89)) when the relative bulk permittivities are $\varepsilon_0 = 1.0,\ \varepsilon_1 = 2.0,\ \varepsilon_2 = 3.0,\ \varepsilon_3 = 4.0$ and; when $\Delta\varepsilon = 0$ (Fig. 3a); when $\Delta\varepsilon = .4,\ \alpha = 5.5,\ \Lambda = 0$ (Fig. 3b); and when $\Delta\varepsilon = .4,\ \alpha = 5.5,\ \Lambda = 4\pi$ (Fig. 3c). We note that considerable algebra involving the bipolar coordinates of Eq. (1) is needed (details not given) to mathematically implement the $\varepsilon(X_1, Y_1)$

function specified from $\varepsilon(u, v)$ of Eq. (89) and shown in Figs. 3a,b, and 3c. The $\varepsilon(u, v)$ profile of Eq. (89) on any bipolar circle of constant u, $-\pi \leq v \leq \pi$, may be called a combined uniform step-cosine profile, since part of the profile is constant for those values of v which are in Reg. 2 and a cosine profile for those values of v which are in Reg. 1.

We now present the electromagnetic fields that result for the second example which was just described for the case when a plane wave is incident (assuming incidence angles either $\phi_0 = 0°$ or $\phi_0 = 180°$) on the system (see Fig. 2) and when the parameter $\Delta\varepsilon$ in Eq. (89) is taken to have a value $\Delta\varepsilon = 0$ (see Fig. 3a). We note for this case that the material in Regs. 1 and 2 are uniform and thus this case represents a case when the KPE [22] method may be used to directly to validate the RCWA algorithm. Figs. 4a and 4b show respectively as a function of the coordinates X_1, Y_1 for $\phi_0 = 0°$, the real part of the electric field E_z, namely $E_{zR} = \mathrm{Re}al(E_z)$, when the KPE method [22] is used to calculate E_{zR} (Fig. 4a) and when the RCWA method was used to calculate E_{zR} (Fig. 4b). In viewing these plots, visually no difference can be seen between the two plots. The KPE plot of Fig. 4a was computed by using $N = 40$ ($m = 0, \ldots, 39$) Hankel-Bessel functions modes and was labeled "Exact" because it was determined through numerical testing that the KPE algorithm had completely converged for this number of modes. Fig. 4b was computed using $N = 30$ state variable modes and using $L = 4200$ layers. Figs. 5a and 5b show the imaginary part of the electric field E_z, namely $E_{zI} = \mathrm{Im}ag(E_z)$, for the same parameters as were shown in Figs. 4a and 4b. Again in viewing these plots, visually no difference can be seen between the two plots. Figs. 6 and 7 show the real part of the magnetic fields $U_{xR} = \mathrm{Re}al(\tilde{\eta}_f H_x)$ and $U_{yR} = \mathrm{Re}al(\tilde{\eta}_f H_y)$, respectively, that are associated with the electric field plots of Figs. 4 and 5. Again in viewing these magnetic field plots, visually no difference can be seen between the KPE and RCWA U_{xR} plots and U_{yR} plots. Rectangular components of the magnetic field have been plotted because the geometry of the scattering systems is a mixture of cylindrical, bipolar and rectangular coordinate systems, thus rectangular components and coordinates are the most convenient ones to use to represent the fields in all regions. In viewing these magnetic field plots of Figs. 6a and 6b and 7a and 7b one notices that for both the U_{xR} and U_{yR} plots, that the magnetic field component is continuous through the plots. This is to be expected since a uniform value of the magnetic permeability was assumed in all regions of space. One also notices in Figs. 6a and 6b that the U_{xR} field is zero on the line $Y_1 = 0$. This is to be expected because the scattering system is symmetric with respect to the Y_1 axis as mentioned earlier.

Figs. 8a and 8b show the real part of the electric field E_{zR} for the

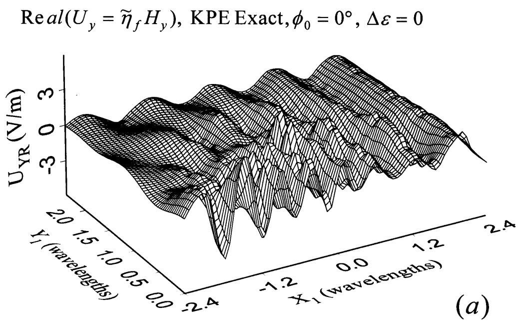

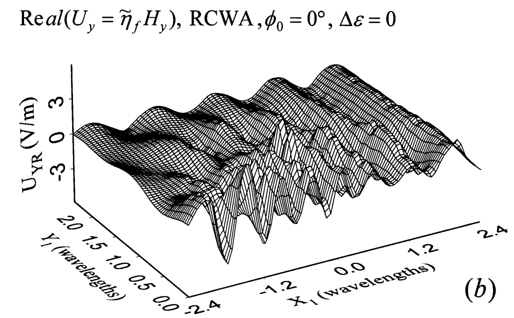

Figure 7. Figs. a and b show for the same case described in Fig. 4, the real part of the magnetic field $U_y = \tilde{\eta}_f H_y$, U_{yR}, that results when the KPE method [22] is used to calculate (Fig. a) and when the RCWA method was used to calculate U_{yR} (Fig. b).

same parameters as were used to make the plots of Figs. 4–7 except that the angle of incidence was taken to be $\phi_0 = 180°$ rather than $\phi_0 = 0°$. In viewing these electric field plots, visually no difference can be seen between the KPE (Fig. 8a) and RCWA (Fig. 8b) plots. It is interesting to note in comparing the field patterns of Fig. 4 ($\phi_0 = 0°$) with those of Fig. 8 ($\phi_0 = 180°$), that totally different electric field patterns arise for the two different angles of incidence. In the Fig. 4 ($\phi_0 = 0°$) case, a more fully developed wave structure is seen, whereas in Fig. 8 ($\phi_0 = 180°$), a much more ripple like pattern occurs than did in Fig. 4 plot, particularly inside the scattering structure.

We would like to mention that plots similar to those of Figs. 4–8 have been made for cases when a lower number of modes and a lower number of layers were used in the RCWA algorithm. It was found in these cases, that visually, just as is seen in Figs. 4–8, that virtually no

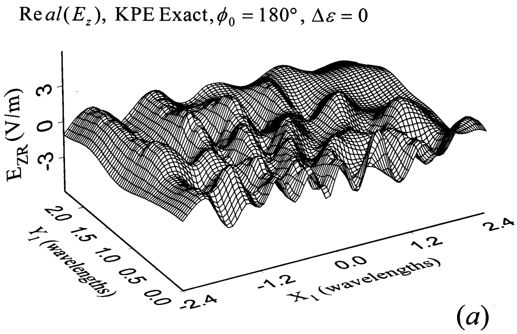

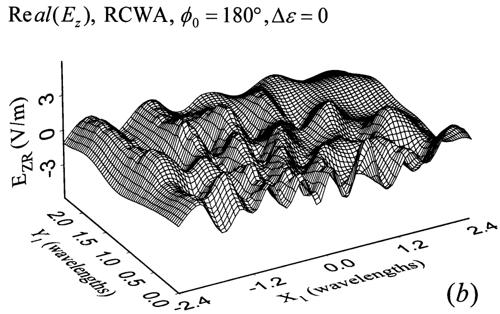

Figure 8. Figs. a and b show, respectively, for the scattering example described in Figs. 1,2,3a and Sec. 3 for $\phi_0 = 180°$, the real part of the electric field E_z, E_{zR}, that results when the KPE method [22] is used to calculate E_{zR} (Fig. a) and when the RCWA method was used to calculate (Fig. b).

difference between KPE and RCWA methods could be observed. For this reason in order to study the convergence of the RCWA method in more detail, two error analyses were made, one which studied the peak difference in the electric and magnetic field values between the KPE and RCWA methods over a given X_1, Y_1 region call it R_1, and the second which studied the root mean square differences between the methods for the same region R_1 and same cases. The peak difference was studied by defining the relative peak error difference measure

$$E_{rel}^{\text{peak}} = 100 \times \frac{\underset{R_1}{Max} \left| F - F_{\text{KPE}^*}^{\text{exact}} \right|}{\underset{R_1}{Max} \left| F_{\text{KPE}^*}^{\text{exact}} \right|} (\%) \tag{90}$$

where; F is any of complex field values E_z, U_x, U_x which have been computed by the RCWA method or by the KPE method (when the

KPE method used a lower number of modes than was used for $F_{\text{KPE}^*}^{\text{exact}}$), $F_{\text{KPE}^*}^{\text{exact}}$ is any of complex field values E_z, U_x, U_x which have been computed by the KPE Exact method using 40 modes (called KPE* in Eq. (90)), represents the magnitude of a complex number, and the Max and R_1 in Eq. (90) means to find the maximum value over the region R_1. The RMS relative difference error measure, E_{rel}^{RMS}, is given by Eq. (90) when the numerator of the second factor in Eq. (90) is replaced by the standard RMS formula $\{\frac{1}{N_s}\sum_{p=1}^{N_s}|F_p - F_{\text{KPE}^*}^{p,\text{exact}}|^2\}^{1/2}$ where p the represents a sample of the complex fields F and $F_{\text{KPE}^*}^{\text{exact}}$ at a point P in region R_1, and where N_s represents the number of samples made over the region R_1. In the present paper the region R_1, for both the peak and RMS error measures, was taken to be the X_1, Y_1 plane shown in Figs. 4–8. For both the peak and RMS error measures, a very fine rectangular, sample grid consisting of $N_s = 240 \times 120$, nearly uniformly spaced, X_1, Y_1 points was used to compute the numerical errors. We say nearly uniformly spaced because when sampling the EM fields inside the inhomogeneous region on an exactly uniform rectangular grid at a point X_1^{rec}, Y_1^{rec}, the field point X_1, Y_1 that was actually used was the point X_1, Y_1 which was on a $\rho_u = r_u,\ u = u_\ell,\ \ell = 1, \ldots, L-1$, internal bipolar circle which was closest in distance to the X_1^{rec}, Y_1^{rec} point. This point was used because, as discussed in Sec. 2, the cylindrical Fourier, electric and magnetic coefficients $E_m(r_u),\ U_m(r_u)$, of $\cos(m\phi_u)$ were computed exactly on the internal layer interfaces $\rho_u = r_u,\ u = u_\ell,\ \ell = 1, \ldots, L-1$ by the matrix multiplication of $\underline{\underline{K_{r_u;r_3}^{SV}}}$ times the matrix $\underline{W^{(3)}}$ which contained the Fourier coefficients $\overline{E_m^{(3)}}(r_3^-),\ U_m^{(3)}(r_3^-)$. Thus by choosing the X_1, Y_1 point on the $\rho_u = r_u,\ u = u_\ell$, interface, the most accurate calculation of the internal EM fields possible was made. This was particularly important in the present example because the EM field summations involved a large number of Fourier harmonics, and thus even a very small spatial displacement between the point X_1^{rec}, Y_1^{rec} of a perfectly uniform spaced rectangular grid and those of a point X_1, Y_1 on the interface, $\rho_u = r_u,\ u = u_\ell,\ \ell = 1, \ldots, L-1$ where the RCWA harmonics were actually computed, could make a relatively large difference in the complex values (particularly the complex phase angle) of the EM field solutions which were being evaluated.

Table 1 shows for the E_z, H_x, H_y components, the % Peak Relative Error with the Exact KPE solution [22] (the Exact KPE solution is labeled KPE* in Table 1), E_{rel}^{peak}, as results: when the KPE solution is calculated using 22, 26 and 30 modes: when the RCWA method is calculated using; 22 modes, 2800 layers; 26 modes, 2800 layers; and 30 modes, 4200 layers for the cases when the angle of

Table 1. The % Peak Relative Error with the Exact KPE solution, E_{rel}^{peak}, is displayed for the E_z, H_x, H_y components for several different computational cases. The Exact KPE solution (40 mode) is labeled KPE*. Also listed is the backscatter width, $\sigma_b = \sigma(\phi_0, \phi_0)$, that result for the KPE and RCWA methods.

Method ($\Delta\varepsilon = 0$)	# Modes, #Layers	ϕ_0 Angle of Inc.	E_z (% Peak Rel. Error with KPE*)	H_x (% Peak Rel. Error with KPE*)	H_y (% Peak Rel. Error with KPE*)	Backscatter Width $\sigma_b = \sigma(\phi_0, \phi_0)$
KPE* (Exact Soln)	40	0°	0.0	0.0	0.0	(4.95907)
KPE	22	0°	4.4564	5.8828	4.2741	4.95919
RCWA	22,2800	0°	4.4834	5.9464	4.2980	4.95545
KPE	26	0°	0.3702	0.7270	0.5074	4.95907
RCWA	26,2800	0°	0.3790	1.2108	0.7035	4.95933
KPE	30	0°	0.0128	0.0333	0.0224	4.95907
RCWA	30,4200	0°	0.2256	1.0280	0.4694	4.95901
KPE* (Exact Soln)	40	180°	0.0	0.0	0.0	(4.38545)
KPE	22	180°	4.2371	5.2686	4.6176	4.38527
RCWA	22,2800	180°	6.2794	8.3671	5.1142	4.11560
KPE	26	180°	0.3517	0.5722	0.5482	4.38545
RCWA	26,2800	180°	0.4094	1.5942	0.6391	4.35349
KPE	30	180°	0.0132	0.0261	0.0244	4.38545
RCWA	30,4200	180°	0.2671	1.2189	0.5668	4.36584

incidence is $\phi_0 = 0°$ and $\phi_0 = 180°$. As can be seen from Table 1, for both the KPE and RCWA methods, that the peak relative error with KPE*, E_{rel}^{peak}, decreases rapidly as the number of modes used increases from 22, to 26, to 30 modes for both angles of incidence $\phi_0 = 0°$ and $\phi_0 = 180°$. It is also observed for both $\phi_0 = 0°$ and $\phi_0 = 180°$ for the KPE method, that for 30 modes, for all the field components E_z, H_x, H_y, that the peak relative error E_{rel}^{peak}, is extremely small, on the order 0.02 to 0.03%. With this extremely small peak error, the present author feels confident that the KPE solution has completely converged when calculated by using 40 modes and that labeling the 40 mode KPE solution as the exact solution KPE* in Table 1 is very justified.

It is also interesting to note that for the 22 and 26 mode

Table 2. The % RMS Relative Error with the Exact KPE solution, E_{rel}^{RMS}, is displayed for the E_z, H_x, H_y components for the same case as Table 1. Also listed is backscatter width, $\sigma_b = \sigma(\phi_0, \phi_0)$, that result for the KPE and RCWA methods.

Method ($\Delta\varepsilon = 0$)	# Modes, #Layers	ϕ_0 Angle of Inc.	E_z (% RMS Rel. Error with KPE*)	H_x (% RMS Rel. Error with KPE*)	H_y (% RMS Rel. Error with KPE*)	Backscatter Width $\sigma_b = \sigma(\phi_0, \phi_0)$
KPE* (Exact Soln)	40	0°	0.0	0.0	0.0	(4.95907)
KPE	22	0°	0.4934	0.5726	0.3697	4.95919
RCWA	22,2800	0°	0.5641	0.7126	0.4251	4.95545
KPE	26	0°	0.0300	0.0453	0.0291	4.95907
RCWA	26,2800	0°	0.0715	0.1312	0.0738	4.95933
KPE	30	0°	0.0008	0.0016	0.0010	4.95907
RCWA	30,4200	0°	0.0426	0.0081	0.0045	4.95901
KPE* (Exact Soln)	40	180°	0.0	0.0	0.0	(4.38545)
KPE	22	180°	0.6189	0.6971	0.4610	4.38527
RCWA	22,2800	180°	1.3355	1.5614	1.0870	4.11560
KPE	26	180°	0.0285	0.0357	0.0315	4.38545
RCWA	26,2800	180°	0.1081	0.1520	0.1018	4.35349
KPE	30	180°	0.0008	0.0012	0.0011	4.38545
RCWA	30,4200	180°	0.0622	0.0853	0.0569	4.36584

calculations, that the KPE and RCWA solutions are showing very similar peak relative error differences (approximately 4 to 8% for the 22 mode case and 0.3 to 1.5% for the 26 mode case) with the exact KPE* solution for both angles of incidence tested and for all field components. It is very reasonable that the number of modes should be an important factor in determining the accuracy of the solutions regardless of whether the KPE or RCWA method is used. It is not surprising that the KPE method is always closer to the exact KPE* solution since for a given number of modes, the Bessel addition formulas used by [22], express exactly the modal coefficients from the inner ($\rho_3 = r_3$) to outer ($\rho_1 = r_1$) layers in terms of Bessel functions, whereas the RCWA method always requires a SV matrix whose matrix elements are constant in each layer, and therefore represents only an approximate EM solution in each thin layer, thus leading to less accurate results than the KPE method can provide.

Table 1 in the last column lists the backscatter width, $\sigma_b =$

$\sigma(\phi_0, \phi_0)$, that result for the KPE and RCWA methods for the different computation cases which have been discussed earlier. One notices for the $\phi_0 = 0°$ case, that σ_b converges very rapidly to the KPE* exact solution (listed in Table 1 in parantheses) when using 22,26,30 modes, for both the RCWA and KPE methods. One notices for the $\phi_0 = 180°$ case, however, that KPE method converges rapidly to the exact σ_b value when using 22,26,30 modes, but that significant error in calculating σ_b arises for the 22 mode case when using the RCWA method, but that more accurate σ_b RCWA results are found when the RCWA method uses 26 and 30 modes. Table 2 lists E_{rel}^{RMS}, the % RMS Relative Error with the Exact KPE* solution as defined earlier, for same cases that were discussed earlier in Table 1. As can be seen by inspecting Table 2, all of the trends discussed for Table 1 are seen again in Table 2. One notices in Table 2, the RMS relative error is much smaller than the peak relative errors of Table 1. This is not surprising since peak error is a much more severe test of accuracy than an RMS error which tends to average out places where relatively large error might occur.

Figs. 9a and 9b for $\phi_0 = 0°$, show, respectively, the real ($E_{zR} = \mathrm{Re}al(E_z)$) and imaginary ($E_{zI} = \mathrm{Im}ag(E_z)$) parts of the electric field E_z for the same parameter case as were shown in Fig. 4 except that $\Delta\varepsilon = 0.4$, $\alpha = 5.5$, and $\Lambda = 0$ rather than $\Delta\varepsilon = 0$. Fig. 3b shows a plot of $\varepsilon(X_1, Y_1)$ (from $\varepsilon(u, v)$ of Eq. (89)) for this example. In this example, because $\Delta\varepsilon$ is not zero in Eq. (89), Reg. 1 is not a uniform material and thus the KPE algorithm cannot be used to calculate the EM fields of the system. The EM fields for the plots of Figs. 9a and 9b were made using 30 modes and using 4200 layers. A comparison of the Fig. 9a plot (E_{zR}, $\Delta\varepsilon = 0.4$, $\alpha = 5.5$, $\Lambda = 0$) and Fig. 4b (E_{zR}, $\Delta\varepsilon = 0$,) shows that Fig. 9a has a very similar field pattern to that shown in Fig. 4b, but on careful inspection of the two plots, one still notices perceptible difference between the two plots. For example, near the origin of the two plots, one notices that in Fig. 9a, a higher peak to peak interference pattern of the E_{zR} field occurs than did in the Fig. 4b plot. A comparison of the Fig. 9b plot (E_{zI}, $\Delta\varepsilon = 0.4$, $\alpha = 5.5$, $\Lambda = 0$) and Fig. 5b (plot of E_{zI}, $\Delta\varepsilon = 0$,) shows that Fig. 9b has a very similar field pattern to that shown in Fig. 5b, but still one may observe perceptible differences between the plots. Overall the presence of the non uniform dielectric material in Reg. 1 of the system cause a definite change in the EM field pattern as to when the material is uniform.

Fig. 10a shows a comparison of the plots of the *db* bistatic scattering width $\sigma_{db}(\phi, \phi_0)$ given by $\sigma_{db}(\phi, \phi_0) \equiv 10 \log(\sigma(\phi, \phi_0))$ as a function of ϕ, the scattering angle, for the model described in Fig. 2 for the case $\phi_0 = 0°$ when $\Delta\varepsilon = 0$ ($\varepsilon(X_1, Y_1)$ shown in Fig. 3a) as

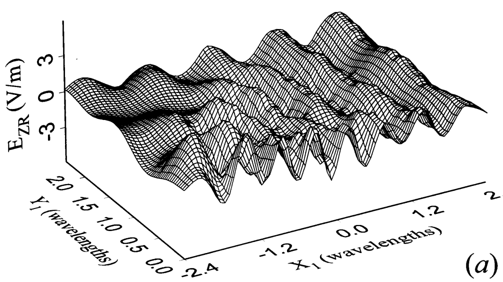

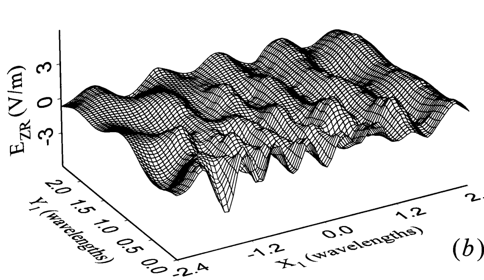

Figure 9. Figs. a and b show for $\phi_0 = 0°,\ \Delta\varepsilon = 0.4,\ \alpha = 5.5,\ \Lambda = 0$, the real (Fig, a) and imaginary (Fig. b) parts of the electric field E_z that result when using the RCWA method. Please note, that because $\Delta\varepsilon \neq 0$ in this case, Reg. 1 is nonuniform, thus only the RCWA may be used to determine EM fields of the system.

calculated by the KPE method using 40 modes (*dot* in Fig. 10a) and as calculated by the RCWA method using 30 modes and 4200 layers (*solid line* in Fig. 10a). As can be seen from the Fig. 10a plots, extremely close numerical results occur by using the two methods. The close agreement of KPE and RCWA method provides further validation of the RCWA method when the material is uniform. Fig. 10b presents a plot of $\sigma_{db}(\phi, \phi_0)$ as a function of ϕ for the model described in Fig. 2 for the case when $\Delta\varepsilon = 0.4,\ \alpha = 5.5,\ \Lambda = 0$ ($\varepsilon(X_1, Y_1)$ shown in Fig. 3b) for $\phi_0 = 0°$ as calculated by the RCWA method using 30 modes and 4200 layers (*solid line* in Fig. 10b). Also shown in Fig. 10b for comparison is the KPE Exact (40 mode) solution (*dashed line*, $\Delta\varepsilon = 0$). As discussed earlier the $\Delta\varepsilon = 0.4,\ \alpha = 5.5,\ \Lambda = 0$ case is one which cannot be analyzed by the KPE method. In comparing the

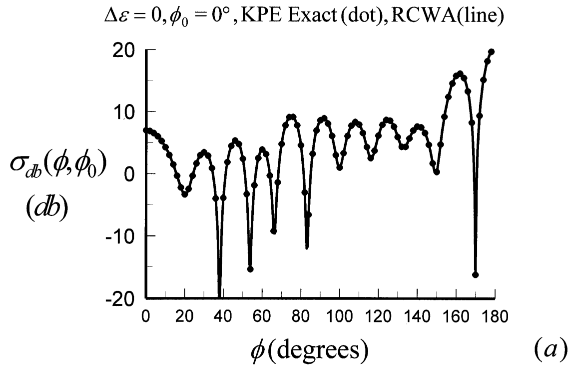

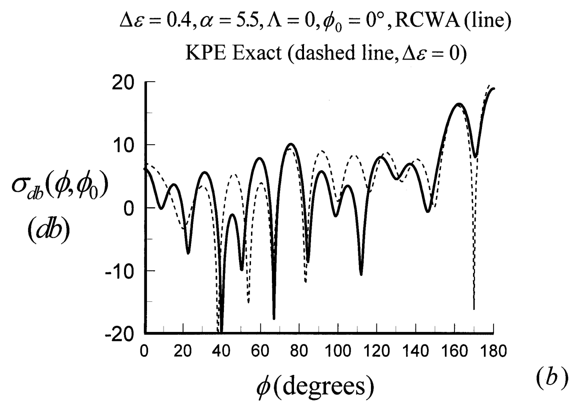

Figure 10. Fig. a shows a comparison of the plots of the $\sigma_{db}(\phi, \phi_0)$ bistatic scattering widths (in *db*) as a function of ϕ for the scattering model described in Figs. 1, 2, 3a and Sec. 3 for the case when (Fig. 3a) $\Delta\varepsilon = 0$ and when $\phi_0 = 0°$, as calculated by the KPE method [22] using 40 modes (*dot* in Fig. a) and as calculated by the RCWA method using 30 modes and 4200 layers (*solid line* in Fig. a). Fig. b shows $\sigma_{db}(\phi, \phi_0)$ for the same case as Fig. a, except $\Delta\varepsilon = 0.4$, $\alpha = 5.5$, $\Lambda = 0$ ($\varepsilon(X_1, Y_1)$ shown in Fig. 3b). Also shown in Fig. b for comparison is the KPE Exact (40 mode) solution (*dashed line*, $\Delta\varepsilon = 0$).

plots (*solid line* and *dashed line*) of Figs. 10b one clearly sees significant differences between the profiles. Figs. 11a and 11b show a comparison of the plots of the *db* bistatic scattering width $\sigma_{db}(\phi, \phi_0)$ as a function of ϕ for the same cases as Figs. 10a,b except that $\phi_0 = 180°$ rather than $\phi_0 = 0°$. In Fig. 11a extremely good validation of the RCWA is seen. In the Fig. 11b plot, the presence of the nonuniform material in Reg. 1 in the scattering model causes a significantly different bistatic

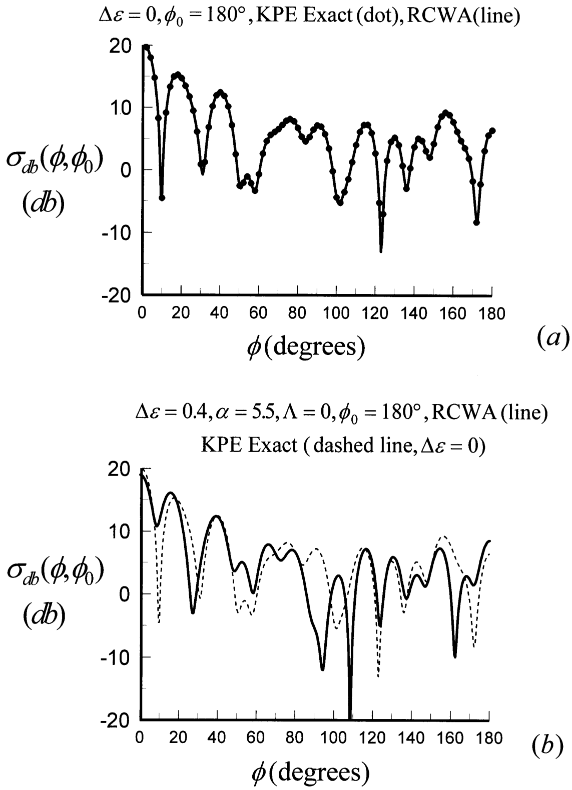

Figure 11. This figure shows $\sigma_{db}(\phi, \phi_0)$ for the same cases as displayed in Fig. 10 except $\phi_0 = 180°$ rather than $\phi_0 = 0°$.

scattering width profile to occur (*solid line* in Fig. 11b) as when the material is uniform (*dashed line*, $\Delta\varepsilon = 0$, Fig. 11b). Overall, for angles of incidences $\phi_0 = 0°$ and $\phi_0 = 180°$, the presence of the non uniform material in Reg. 1 (see Figs. 2 and 3b) produces a significantly different bistatic scattering width profile (*solid line* Figs. 10b and 11b) than when the Reg. 1 material is uniform (*dashed line*, Figs. 10b and 11b).

Fig. 12a shows a comparison of the plots of the *db* bistatic scattering width $\sigma_{db}(\phi, \phi_0)$ as a function of ϕ for the model of the second example described earlier (see Fig. 2) for the case when $\Delta\varepsilon = 0.4$, $\alpha = 5.5$, $\Lambda = 4\pi$ (($\varepsilon(X_1, Y_1)$ shown in Fig. 3c), $\phi_0 = 0°$ as calculated by the RCWA method using 30 modes and 4200 layers (*solid line* in Fig. 12a). Also shown for comparison is the KPE exact solution (*dashed line* in Fig. 12a). As can be seen from the Fig. 12a plots, the presence of the material inhomogeneity in Reg. 1 (see Fig. 2) causes a

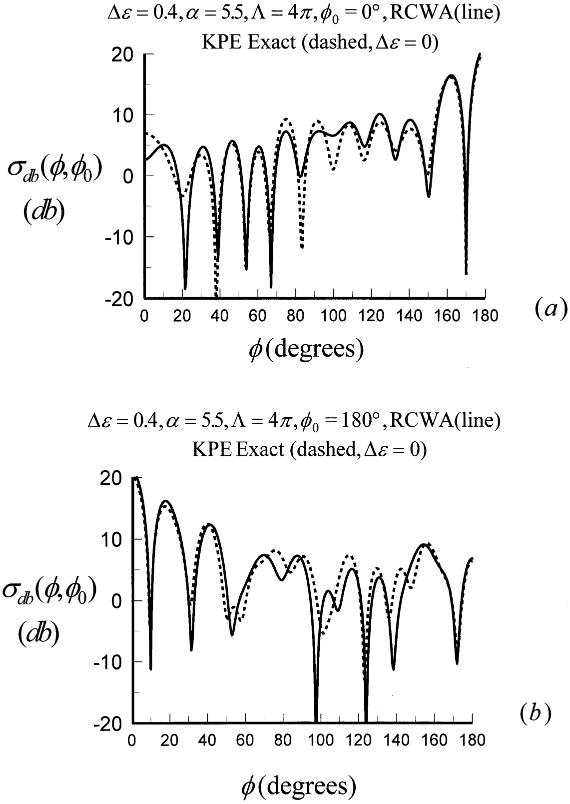

Figure 12. Fig. a shows a comparison of the plots of given as a function of $\sigma_{db}(\phi, \phi_0)$ for the scattering model described in Figs. 1, 2, 3c and Sec. 3 for the case when $\Delta\varepsilon = 0.4,\ \alpha = 5.5,\ \Lambda = 4\pi$ (corresponding to Fig. 3c) when $\phi_0 = 0°$ as calculated by the RCWA method (*solid line* in Fig. a). Also shown for comparison is the KPE exact solution (*dashed line* in Fig. a). Fig. b shows $\sigma_{db}(\phi, \phi_0)$ for the same case as Fig. a, except $\phi_0 = 180°$ rather than $\phi_0 = 0°$.

perceptible difference in the bistatic scattering width as compared to the case when Reg. 1 is uniform. Fig. 12b shows a plot of the bistatic scattering width for the same cases as Fig. 12a except that the angle of incidence has been taken to be $\phi_0 = 180°$ rather than $\phi_0 = 0°$. Again one notices, the presence of the material inhomogeneity in Reg. 1 (see Fig. 2) causes a perceptible difference in the bistatic scattering width as compared to the case when Reg. 1 is uniform. It is interesting to note that in comparing Figs. 10b and 12a (both $\phi_0 = 0°$), that the inhomogeneity used in Fig. 10b ($\Delta\varepsilon = 0.4,\ \alpha = 5.5,\ \Lambda = 0$, Fig. 3b) caused a larger difference with the uniform region cases than did the inhomogeneity ($\Delta\varepsilon = 0.4,\ \alpha = 5.5,\ \Lambda = 4\pi$, Fig. 3c) used in Fig. 12a. This is not surprising, because although the inhomogeneity used in Fig. 12a had a more rapid spatial variation overall than the one used in Fig. 10a, its radial u variation nevertheless tended to average out the EM field, thus producing less marked difference with the uniform region case than did the inhomogeneity used in Fig. 12a. Overall in Figs. 10b, 11b, 12a and 12b, the differences between the uniform material case (*dashed line*) and nonuniform material case (*solid line*), are very believable and are of the order one would expect for the inhomogeneity profiles shown in Figs. 3b and 3c.

For the case when the permittivity of the material between the interfaces is nonuniform (i.e., when $\Delta\varepsilon \neq 0$) it is not possible to use the KPE algorithm to validate numerical results. As mentioned at the end of Sec. 2, one possible way to at least partially validate the RCWA algorithm for this case is to solve a system matrix equation which is based on a mixed combination of outward and inward transfer matrices, and then compare the numerical results of this algorithm with the main RCWA algorithm of the paper, namely the algorithm based on a pure outward transfer matrix. Table 3 shows the error results of such an analysis where the mixed transfer matrix method is entitled RCWAm and was based on the use of a outward transfer matrix $\underline{\underline{Z}}{}^{SV}_{r_u;r_3}$ and on the use of a inward transfer matrix $\underline{\underline{Z}}{}^{SV}_{r_1;r_u}$ (r_u is located $.75L$ # of layers outward from r_3 and $.25L$ # of layers inward from r_1) to formulate the matrix equation of the overall system. The error measure was obtained by replacing $F^{\text{exact}}_{\text{KPE}^*}$ in Eq. (90) with $F^{\text{out}}_{\text{RCWA}^*}$, where $F^{\text{out}}_{\text{RCWA}^*}$ is any of the complex field values E_z, U_x, U_x which have been computed by the RCWA method which was based on a pure outward transfer method using 30 modes and 4200 layers, and taking F in Eq. (90) to be any of the EM fields calculated by the RCWAm method. All EM fields associated with the RCWAm method were calculated from the electric and magnetic Fourier coefficients which were found from the matrix solution at the $\rho_3 = r_3$ boundary. The region R_1 used for Table 3 is the same one used for Tables 1 and 2. In Table 3, the first set of data, corresponding to $\Delta\varepsilon = 0$, shows the relative peak error E^{peak}_{rel} for E_z, H_x, H_y between the RCWA* and RCWAm algorithms for different numbers of modes and layers and for $\phi_0 = 0^\circ, 180^\circ$. In this set of data one clearly sees the peak error between the two RCWA algorithm solutions decreases as the number of modes and layers increases. The rate of error reduction with increase in the number of modes is very similar to that seen in the Table 1 relative peak error data when the KPE and RCWA algorithm solutions were

Table 3. The % Peak Relative Error E_{rel}^{peak} between the RCWA* algorithm (based a pure outward transfer matrix) and the RCWAm algorithm (based on the use of a 3/4 outward and 1/4 inward transfer matrix) is displayed for the E_z, H_x, H_y components for different computational cases. Also listed is backscatter width, $\sigma_b = \sigma(\phi_0, \phi_0)$, that result for the KPE Exact (40 mode), RCWA and RCWAm methods.

Method, $\Delta\varepsilon, \alpha, \Lambda$	# Modes, #Layers	ϕ_0 Angle of Inc.	E_z (% Peak Rel.Error with RCWA*)	H_x (% Peak Rel. Error with RCWA*)	H_y (% Peak Rel. Error with RCWA*)	Backscatter Width $\sigma_b = \sigma(\phi_0, \phi_0)$
$\Delta\varepsilon = 0$						
KPE* (Exact)	40	0°				(4.95907)
RCWA*	22,2800	0°	0.0	0.0	0.0	4.95545
RCWAm	22,2800	0°	1.2193	2.3026	.7540	4.94900
RCWA*	26,2800	0°	0.0	0.0	0.0	4.95933
RCWAm	26,2800	0°	0.1991	0.2552	0.1785	4.95702
RCWA*	30,4200	0°	0.0	0.0	0.0	4.95901
RCWAm	30,4200	0°	0.1232	0.1541	0.1084	4.95744
KPE* (Exact)	40	180°				(4.38545)
RCWA*	22,2800	180°	0.0	0.0	0.0	4.11560
RCWAm	22,2800	180°	3.5397	6.0937	2.3769	4.16989
RCWA*	26,2800	180°	0.0	0.0	0.0	4.39533
RCWAm	26,2800	180°	0.4259	0.7202	0.4219	4.39533
RCWA*	30,4200	180°	0.0	0.0	0.0	4.36584
RCWAm	30,4200	180°	0.2422	0.3034	0.2249	4.39421
$\Delta\varepsilon = 0.4, \alpha = 5.5,$ $\Lambda = 0$						
RCWA*	30,4200	0°	0.0	0.0	0.0	4.09170
RCWAm	30,4200	0°	0.6920	1.1630	0.7738	4.09625
RCWA*	30,4200	180°	0.0	0.0	0.0	7.12139
RCWAm	30,4200	180°	0.7489	1.7432	0.9104	7.16171
$\Delta\varepsilon = 0.4, \alpha = 5.5,$ $\Lambda = 4\pi$						
RCWA*	30,4200	0°	0.0	0.0	0.0	1.82968
RCWAm	30,4200	0°	0.2358	0.3970	0.2542	1.83414
RCWA*	30,4200	180°	0.0	0.0	0.0	4.79632
RCWAm	30,4200	180°	0.2257	0.3625	0.2230	4.82439

compared with the KPE* Exact (40 mode) solution. The second and third sets of data in Table 3 show the peak error difference E_{rel}^{peak} for the two inhomogeneous material examples corresponding to Figs. 3b and 3c respectively for just the case when 30 modes and 4200 layers have been used in both RCWA algorithms for $\phi_0 = 0°, 180°$. In comparing all three data sets for 30 modes and 4200 layers, one notices that relative peak error E_{rel}^{peak} for the second data set ($\Delta\varepsilon = 0.4,\ \alpha = 5.5,\ \Lambda = 0$) is clearly larger ($E_{rel}^{\text{peak}} \cong 1$ to 2%) than that of the first ($\Delta\varepsilon = 0$) and third ($\Delta\varepsilon = 0.4,\ \alpha = 5.5,\ \Lambda = 4\pi$) data sets where the error is $E_{rel}^{\text{peak}} \cong 0.1$ to 0.4%. This result seems very much in line with observations made that the difference in the bistatic scattering widths seen in Figs. 10b and 11b (comparison of $\Delta\varepsilon = 0$, Fig. 3a (*dashed line*) with $\Delta\varepsilon = 0.4,\ \alpha = 5.5,\ \Lambda = 0$, Fig. 3b (*solid line*)) was greater than was the difference seen in Figs 12a and 12b (comparison of $\Delta\varepsilon = 0$, Fig. 3a (*dashed line*) with $\Delta\varepsilon = 0.4,\ \alpha = 5.5,\ \Lambda = 4\pi$, Fig. 3c (*solid line*)).

4. SUMMARY, CONCLUSIONS, AND FUTURE WORK

The paper has presented a bipolar RCWA algorithm for the calculation of EM fields and scattering from an inhomogeneous material, composite, eccentric, circular, cylinder system. The basic RCWA formulation in bipolar coordinates has been presented as well as a complete description of the boundary matching equations that were used. Extensive use of the residue theorem to calculate various bipolar interaction integrals (Appendix A) allowed an extremely accurate and fast numerical implementation of both the RCWA formulation and the boundary matching equations. The RCWA algorithm was extensively validated using an algorithm developed by [22] to study scattering from uniform material eccentric cylinders (termed the KPE algorithm in this paper). For validation purposes the paper presented a slightly altered formulation of the KPE algorithm (Appendix B) which allowed the transfer matrices of the RCWA and KPE algorithms to be compared. Numerical validation results of the RCWA algorithm were presented in the text directly, were presented in Figs. 4–8, 10a, and 11a and were presented in Tables 1, 2, and 3. In the author's opinion extremely close numerical results for the between the KPE and RCWA algorithms were observed. In Figs. 9, 10b, 11b, 12a and 12b numerical examples involving inhomogeneous materials were presented. Very reasonable numerical results were obtained. In this paper RCWA was applied only to case where the EM fields and scattering object were symmetric with respect to y coordinate. We would like to mention that the extension of the RCWA algorithm to the case where the EM fields and a scattering object have arbitrary symmetry is straight forward.

There are several areas for which the RCWA algorithm that has been presented could be improved. One area concerns the numerical calculation of the eigenvalues and eigenfunctions of the RCWA algorithm. Numerical testing has shown that in determining the SV modes, that the higher the mode number and the larger the magnitude of the eigenvalue Q_n, that the coefficients of the eigenfunction $S_{zn}(v)$ for that mode, have a certain integer index value call it $i_{n,\max}$, for which the magnitude of the coefficient is largest. As one calculates the magnitude of the Fourier coefficients $S_{z\mathrm{in}}(v)$ of S_{zn} (Eq. (17)) for integer values above or below this value, the magnitudes of the adjacent coefficients die off more and more rapidly as the magnitude of Q_n increases. Put in spectral domain terms, as the magnitude of the eigenvalue Q_n increases, the $S_{zn}(v)$ coefficients which are centered about $i_{n,\max}$, become more and more narrow band. This means that when solving the SV matrix for a given higher order mode, that one might be able to perform an eigenanalysis on a much smaller (or greatly reduced) SV matrix which has been truncated around those matrix elements (i.e., associated with $i_{n,\max}$) which contribute most to the given higher order mode. This would of course save a great deal of computational time, particularly for numerical scattering examples which are much larger than have already been studied. Another area where the RCWA computation time could be greatly reduced is if parallel processing were used to carry out the SV eigenanalysis of the system. The SV eigenanalysis is very amenable to parallel processing since the eigenanalysis in each thin layer may be calculated independently of every other layer. As the eigenanalysis is the most time consuming step in algorithm parallel process would reduce the processing time approximately by a factor of $1/L$ where L is the number of layers.

APPENDIX A.

This appendix will present the calculation of the exponential Fourier coefficients that are used in this paper. We will first determine the Fourier coefficients of the series

$$\exp(-jm\phi_u(u,v)) = \sum_{i=-\infty}^{\infty} \alpha_i^{(-m)}(u) \exp(jiv) \tag{A1}$$

$$\alpha_i^{(-m)}(u) = \frac{1}{2\pi} \int_{-\pi}^{\pi} \exp(-jm\phi_u(u,v) - jiv) dv \tag{A2}$$

where $m \geq 1$, where $u > 0$, where the angle $\phi_u(u, v)$ defined in Eq. (3) is the circular, cylindrical coordinate defined at the center of the O_u circle whose radius is $r_u = a/\sinh(u)$ and whose center is $x_{cu} = a/\tanh(u)$ (see Fig. 1). We first study the function

$$\exp(j\phi_u(u, v)) = \cos(\phi_u(u, v)) + j\sin(\phi_u(u, v)) = (x - x_{cu} + jy)/r_u \tag{A3}$$

where $x = a\sinh(u)/(\cosh(u) - \cos(v))$ and $y = -a\sin(v)/(\cosh(u) - \cos(v))$ are the bipolar coordinates of Eq. (1). Substituting x, y, and x_{cu} into Eq. (A3) one finds after algebra

$$\exp(j\phi_u(u, v)) = \frac{F}{(\cosh(u) - \cos(v))} \tag{A4}$$

$$\begin{aligned} F &= \cosh(u)\cos(v) - 1 - j\sinh(u)\sin(v) \\ &= \frac{1}{2}\exp(-jv)\exp(-u)[\exp(jv) - \exp(u)]^2 \end{aligned} \tag{A5}$$

Algebraic manipulation shows

$$\cosh(u) - \cos(v) = -\frac{1}{2}\exp(-jv)[\exp(jv) - \exp(-u)][\exp(jv) - \exp(u)] \tag{A6}$$

After simplification it is found

$$\exp(j\phi_u(u, v)) = -\exp(-u)\left[\frac{\exp(jv) - \exp(u)}{\exp(jv) - \exp(-u)}\right] \tag{A7}$$

If the $\exp(j\phi_u(u, v))$ is raised to the power $-m$ power and substituted into Eq. (A2) and following the complex variable theory of [23], a substitution $z = \exp(jv)$ is made, it is found that the resulting Eq. (A2) integral is

$$\alpha_i^{(-m)} = \frac{1}{2\pi j}(-1)^m \exp(mu) \oint_{C;|z|=1} \left[\frac{z - \exp(-u)}{z - \exp(u)}\right]^m \frac{dz}{z^{i+1}} \tag{A8}$$

where the substitutions $\exp(-jiv) = z^{-i}$, $dz = j\exp(jv)dv = jzdv$, $dv = dz/jz$ have been made in Eq. (A8), and where $C; |z| = 1$ represents a counter clockwise integration in the complex z plane around the line $|z| = 1$. The factor $\left[\frac{z-\exp(-u)}{z-\exp(u)}\right]^m$ for $m \geq 1$, is analytic in the region of the complex plane $|z| \leq 1$, and the factor z^{i+1} represents a pole of order $i + 1$ for $i > 0$. We thus see using the residue theorem [23] for $m \geq 1$

$$\alpha_i^{(-m)}(u) = (-1)^m \exp(mu)\frac{1}{i!}\left\{\frac{d^i}{dz^i}\left[\frac{z - \exp(-u)}{z - \exp(u)}\right]^m\right\}\Big|_{z=0} \tag{A9}$$

for $i \geq 0$ and $\alpha_i^{(-m)} = 0$ for $i \leq -1$.

For the case when $m = 0$,

$$\alpha_i^{(0)}(u) = \begin{cases} 1, & i = 0 \\ 0, & i \neq 0 \end{cases} \tag{A10}$$

The coefficients $\alpha_i^{(m)}$ for $m \geq 1$ may be found by taking the complex conjugate Eq. (A1) and comparing the coefficients of $\exp(jiv)$ of the two series. The result is for $m \geq 1$ and for all i is

$$\alpha_i^{(m)} = \alpha_{-i}^{(-m)^*} \tag{A11}$$

Since $\alpha_i^{(m)}(u)$ is purely real, the complex conjugate may be omitted. The higher order derivatives in Eq. (A9) may be readily calculated and evaluated by summing the series specified by the Leibniz derivative product rule given in [24]. The validity of Eq. (A9) has been checked for several cases by direct numerical integration of Eq. (A2).

An analysis similar to that performed to calculate the $\alpha_i^{(m)}(u)$ coefficients shows that the $\beta_i^{(-m)}(u)$ coefficients for $u > 0$ for the Fourier series of Eq. (73), Sec. 2, are given by for $m \geq 1$

$$\beta_i^{(-m)}(u) = (-1)^{m+1} \exp(mu) \frac{2}{(i-1)!} \left\{ \frac{d^{i-1}}{dz^{i-1}} \left[\frac{(z-\exp(-u))^{m-1}}{(z-\exp(u))^{m+1}} \right] \right\} \Big|_{z=0} \tag{A12}$$

for $i \geq 1$ and $\beta_i^{(-m)}(u) = 0$ for $i \leq 0$. For $m = 0$ it is found

$$\beta_i^{(0)}(u) = \frac{1}{\sinh(u)} \exp(-|i|u) \tag{A13}$$

for all i. The $\beta_i^{(m)}(u)$ coefficients for $m \geq 1$ are given by for all i by

$$\beta_i^{(m)}(u) = \beta_{-i}^{(-m)}(u)^* \tag{A14}$$

Since $\beta_{-i}^{(-m)}$ is purely real, the complex conjugate may be omitted.

The $\zeta_i^{(m)}(u)$ coefficient of Eq. (33) for $u > 0$ is given by the integral

$$\zeta_i^{(m)}(u) = \frac{1}{2\pi} \int_{-\pi}^{\pi} \left[\frac{d}{dv} \phi_u(u,v) \right] \exp(jm\phi_u(u,v) - jiv) dv \tag{A15}$$

For $m \neq 0$, the $\zeta_i^{(m)}(u)$ coefficient may be calculated from the $\alpha_i^{(m)}(u)$ coefficients as follows. We note for $m \neq 0$,

$$\exp(jm\phi_u(u,v) \frac{d}{dv} \phi_u(u,v) = \frac{1}{jm} \frac{d}{dv} \exp(jm\phi_u(u,v))$$

$$= \frac{1}{jm}\frac{d}{dv}\left[\sum_{i=-\infty}^{\infty}\alpha_i^{(m)}(u)\exp(jiv)\right] \quad \text{(A16)}$$

$$\exp(ji\phi_u(u,v)\frac{d}{dv}\phi_u(u,v) = \sum_{i=-\infty}^{\infty}\frac{i}{m}\alpha_i^{(m)}(u)\exp(jiv) \quad \text{(A17)}$$

For all $m \neq 0$, we find

$$\zeta_i^{(m)}(u) = \frac{i}{m}\alpha_i^{(m)}(u) \quad \text{(A18)}$$

For $m = 0$ it turns out for all i

$$\zeta_i^{(0)}(u) = -\exp(-|i|u) \quad \text{(A19)}$$

The Fourier series for the function $\varepsilon_h(u,v) \equiv h^2(u,v)\varepsilon(u,v)$, Eq. (7), is given by

$$\varepsilon_h(u,v) = \sum_{i=-\infty}^{\infty}\left[\sum_{i'=-\infty}^{\infty}h_{i-i'}^{sq}(u)\varepsilon_{i'}(u)\right]\exp(jiv) \quad \text{(A20)}$$

where $\varepsilon_{i'}(u)$ are the Fourier coefficients of the relative dielectric permittivity function $\varepsilon(u,v)$ and $h_i^{sq}(u)$ are the Fourier coefficient of the squared scale factor function $h^2(u,v)$. Using the residue theorem it may be shown that

$$h_i^{sq}(u) = a^2\exp(-|i|u)\left[\frac{\cosh(u) + |i|\sinh(u)}{\sinh^3(u)}\right] \quad \text{(A21)}$$

for all for all i.

In addition to Eq. (A9), the validity of the other Fourier coefficient formulas presented in this appendix have been checked for several cases by direct numerical integration of the integrals which defined them.

APPENDIX B.

This appendix will give a derivation of the single layer, eccentric circle, Bessel transfer matrix which was described in the main text. The derivation will be based on a modification of the KPE algorithm presented in [22]. We will derive, as a representative example, the transfer matrix for the layer enclosed by the $\rho_1 = r_1$ and $\rho_2 = r_2$ circles of Fig. 2 with the material parameters taken to be $\varepsilon_1 = \varepsilon$ and $\mu_1 = \mu$. Letting $E_z^{(p)}$ and $U_\phi^{(p)} = \tilde{\eta}_f H_\phi^{(p)}$, $p = 1, 2$ be the electric and magnetic fields at the $\rho_1 = r_1^-$ and $\rho_2 = r_2^+$ boundaries respectively we have KPE [22]

$$E_z^{(p)} = \sum_{m=-\infty}^{\infty} \left[A_{em}^{(p)} J_m(X_p) + B_{em}^{(p)} H_2^{(2)}(X_p)\right] \exp(jm\phi_p) \tag{B1}$$

$$U_\phi^{(p)} \equiv \tilde{\eta}_f H_\phi^{(p)} = \frac{k}{j\mu} \sum_{m=-\infty}^{\infty} \left[A_{em}^{(p)} J_m'(X_p) + B_{em}^{(p)} H_2^{(2)'}(X_p)\right] \exp(jm\phi_p) \tag{B2}$$

where $X_p = k\rho_p,\ p = 1, 2,\ k = \sqrt{\mu\varepsilon}$,

$$A_{em}^{(1)} = \sum_{m'=-\infty}^{\infty} Z_{m,m'}^{\exp} A_{em'}^{(2)} \tag{B3}$$

$$B_{em}^{(1)} = \sum_{m'=-\infty}^{\infty} Z_{m,m'}^{\exp} B_{em'}^{(2)} \tag{B4}$$

$$Z_{m,m'}^{\exp} = \exp[j(m' - m)\phi_{12}] J_{m-m'}(ke_{12}) \tag{B5}$$

$$(m, m') = -\infty, \ldots, \infty$$

where $e_{12} = \tilde{k}_f \tilde{e}_{12} > 0$ is the magnitude of the separation distance of the centers of the O_1 and O_2 circles, where $\phi_{12} = 0$ when the O_2 circle center is to the right of the O_1 circle center, and $\phi_{12} = \pi$ when the O_2 circle center is to the left of the O_1 circle center. The subscript "e" in Eqs. (B1)–(B4) represents "exponential". If we take advantage of the symmetry of the present problem and perform algebra we find

$$\begin{aligned} E_z^{(p)} &= \sum_{m=0}^{\infty} \left[A_{cm}^{(p)} J_m(X_p) + B_{cm}^{(p)} H_m^{(2)}(X_p)\right] \cos(m\phi_p) \\ &\equiv \sum_{m=0}^{\infty} E_m(r_p) \cos(m\phi_p) \end{aligned} \tag{B6}$$

$$\begin{aligned} U_\phi^{(p)} &\equiv \tilde{\eta}_f H_\phi^{(p)} = \sum_{m=0}^{\infty} \frac{k}{j\mu} \left[A_{cm}^{(p)} J_m'(X_p) + B_{cm}^{(p)} H_m^{(2)'}(X_p)\right] \cos(m\phi_p) \\ &\equiv \sum_{m=0}^{\infty} U_m(r_p) \cos(m\phi_p) \end{aligned} \tag{B7}$$

where

$$A_{cm}^{(1)} = \sum_{m'=0}^{\infty} Z_{m,m'}^{\cos} A_{cm'}^{(2)} \tag{B8}$$

$$B_{cm}^{(1)} = \sum_{m'=0}^{\infty} Z_{m,m'}^{\cos} B_{cm'}^{(2)} \tag{B9}$$

and

$$Z_{m,m'}^{\cos} = (2-\delta_{0,m}) \begin{cases} Z_{m,m'}^{\exp}, & m'=0 \\ \dfrac{1}{2}\left[(-1)^{m'} Z_{m,-m'}^{\exp} + Z_{m,m'}^{\exp}\right], & m' \geq 1 \end{cases} \tag{B10}$$

and where

$$E_m(\rho_p) = A_{cm}^{(p)} J_m(X_p) + B_{cm}^{(p)} H_m^{(2)}(X_p) \tag{B11}$$

$$U_m(\rho_p) = \frac{k}{j\mu}\left[A_{cm}^{(p)} J_m'(X_p) + B_{cm}^{(p)} H_m^{(2)\prime}(X_p)\right] \tag{B12}$$

where the subscript "c" in Eqs. (B6), (B7) represents "cosine" and has been placed there to distinguish the exponential coefficients of Eqs. (B1)–(B4). For each value of $m = 0, 1, \ldots$, the 2×2 equations in Eqs. (B11), (B12) which specify $E_m(\rho_p)$ and $U_m(\rho_p)$ in terms of $A_{cm}^{(p)}$ and $B_{cm}^{(p)}$, may be inverted to express the $A_{cm}^{(p)}$ and $B_{cm}^{(p)}$ coefficients in terms of the $E_m(\rho_p)$ and $U_m(\rho_p)$ coefficients. These resulting expressions may be further simplified by using the Wronskian relation of Eq. (82) that applies for the $J_m(X_p)$, $H_m^{(2)}(X_p)$, functions. If the $A_{cm}^{(2)}$, $B_{cm}^{(2)}$ coefficients, expressed as 2×2 linear combination of the $E_m(r_2^+)$, $U_m(r_2^+)$ coefficients are substituted in Eqs. (B8), (B9), and if the $A_{cm}^{(1)}$, $B_{cm}^{(1)}$ coefficients, expressed as 2×2 linear combination of the $E_m(r_1^-)$, $U_m(r_1^-)$ coefficients are substituted Eqs. (B11), (B12), the coefficients $E_m(r_1^-)$, $U_m(r_1^-)$ may be expressed in terms of $E_m(r_2^+)$, $U_m(r_2^+)$. The final results are

$$E_m(r_1^-) = \sum_{m'=0}^{\infty}\left[Z_{m,m'}^{BEE} E_{m'}(r_2^+) + Z_{m,m'}^{BEU} U_{m'}(r_2^+)\right] \tag{B13}$$

$$U_m(r_1^-) = \sum_{m'=0}^{\infty}\left[Z_{m,m'}^{BUE} E_{m'}(r_2^+) + Z_{m,m'}^{BUU} U_{m'}(r_2^+)\right] \tag{B14}$$

where

$$Z_{m,m'}^{BEE} = \left[\frac{j\pi}{2} X_2\right]\left[J_m(X_1) H_{m'}^{(2)\prime}(X_2) - H_m^{(2)}(X_1) J_{m'}'(X_2)\right] Z_{m,m'}^{\cos} \tag{B15}$$

$$Z_{m,m'}^{BEU} = \left[\frac{\pi}{2} X_2 \left(\frac{\mu}{k}\right)\right]\left[J_m(X_1) H_{m'}^{(2)}(X_2) - H_m^{(2)}(X_1) J_{m'}(X_2)\right] Z_{m,m'}^{\cos}$$

(B16)

$$Z^{BUE}_{m,m'} = \left[\frac{\pi}{2}X_2\left(\frac{k}{\mu}\right)\right]\left[J'_m(X_1)H^{(2)'}_{m'}(X_2) - H^{(2)'}_{m}(X_1)J'_{m'}(X_2)\right]Z^{\cos}_{m,m'} \tag{B17}$$

$$Z^{BUU}_{m,m'} = \left[\frac{j\pi}{2}X_2\right]\left[-J'_m(X_1)H^{(2)}_{m'}(X_2) + H^{(2)'}_{m}(X_1)J_{m'}(X_2)\right]Z^{\cos}_{m,m'} \tag{B18}$$

for $(m, m') = 0, 1, \ldots, \infty$. The overall transfer matrix is given by this layer is

$$\underline{\underline{Z^B_{r_1;r_2}}} \equiv \begin{bmatrix} \underline{\underline{Z^{BEE}}} & \underline{\underline{Z^{BEU}}} \\ \underline{\underline{Z^{BUE}}} & \underline{\underline{Z^{BUU}}} \end{bmatrix} \tag{B19}$$

where $\underline{\underline{Z^{BEE}}} = \left[\underline{\underline{Z^{BEE}_{m,m'}}}\right]$, etc..

A nice feature of the transfer matrix of Eq. (B19) is the fact that in the case of multi-eccentric cylinders, the overall transfer matrix of the system may be found by the proper cascade matrix multiplication of the transfer matrices of each individual layer. For the two layer example of Fig. 2, assuming in general different materials in each layer, let the single layer transfer matrices be $\underline{\underline{Z^B_{r_2;r_3}}}$ and $\underline{\underline{Z^B_{r_1;r_2}}}$ and let the electric and magnetic field coefficient column matrices be $\underline{E(r_3^+)} = [E_m(r_3^+)]$, $\underline{U(r_3^+)} = [U_m(r_3^+)]$, etc.. We have

$$\begin{bmatrix} \underline{E(r_1^-)} \\ \underline{U(r_1^-)} \end{bmatrix} = \underline{\underline{Z^B_{r_1;r_2}}} \begin{bmatrix} \underline{E(r_2^+)} \\ \underline{U(r_2^+)} \end{bmatrix} \tag{B20}$$

$$\begin{bmatrix} \underline{E(r_2^-)} \\ \underline{U(r_2^-)} \end{bmatrix} = \underline{\underline{Z^B_{r_2;r_3}}} \begin{bmatrix} \underline{E(r_3^+)} \\ \underline{U(r_3^+)} \end{bmatrix} \tag{B21}$$

Because the tangential electric and fields are continuous at the all interfaces, the electric and magnetic coefficients satisfy $E_m(r_j^-) = E_m(r_j^+)$, $U_m(r_j^-) = U_m(r_j^+)$ for $j = 1, 2, 3$ and thus

$$\begin{bmatrix} \underline{E(r_1^+)} \\ \underline{U(r_1^+)} \end{bmatrix} = \underline{\underline{Z^B_{r_1;r_3}}} \begin{bmatrix} \underline{E(r_3^-)} \\ \underline{U(r_3^-)} \end{bmatrix} \tag{B22}$$

where $\underline{\underline{Z^B_{r_1;r_3}}} = \underline{\underline{Z^B_{r_1;r_2}Z^B_{r_2;r_3}}}$. For Fig. 2, $\underline{\underline{Z^B_{r_1;r_3}}}$ is the Bessel transfer matrix which expresses the Bessel coefficients $E_m(r_1^+)$, $U_m(r_1^+)$ in terms of $E_m(r_3^-)$, $U_m(r_3^-)$.

REFERENCES

1. Moharam, M. G. and T. K. Gaylord, "Rigorous coupled-wave analysis of planar grating diffraction," *J. Opt. Soc. Amer.*, Vol. 71, 811–818, 1981.
2. Moharam, M. G. and T. K. Gaylord, "Diffraction analysis of dielectric surface-relief gratings," *J. Opt. Soc. Amer.*, Vol. 72, 1385–1392, 1982.
3. Rokushima, K. and J. Yamakita, "Analysis of anisotropic dielectric gratings," *J. Opt. Soc. Amer.*, Vol. 73, 901–908, 1983.
4. Moharam, M. G. and T. K. Gaylord, "Three-dimensional vector coupled-wave analysis of planar-grating diffraction," *J. Opt. Soc. Amer.*, Vol. 73, 1105–1112, 1983.
5. Glytsis, E. N. and T. K. Gaylord, "Rigorous three-dimensional coupled-wave diffraction analysis of single and cascaded anisotropic gratings," *J. Opt. Soc. Amer. A*, Vol. 4, 2061–2080, 1987.
6. Moharam, M. G., E. B. Grann, D. A. Pommet, and T. K. Gaylord, "Formulation for stable and efficient implementation of rigorous coupled-wave analysis of binary gratings," *J. Opt. Soc. Am. A*, Vol. 12, No. 5, 1068–1076, 1995.
7. Moharam, M. G., D. A. Pommet, E. B. Grann, and T. K. Gaylord, "Stable implementation of the rigorous coupled-wave analysis for surface-relief gratings: enhanced transmittance matrix approach," *J. Opt. Soc. Am. A*, Vol. 12, No. 5, 1077–1086, 1995.
8. Frezza, F., L. Pajewski, and G. Schettini, "Characterization and design of two-dimensional electromganetic band gap structures by use of a full-wave method for diffraction gratings," *IEEE Trans. Micowave Theory and Techniques*, Vol. 51, No. 3 , 941–951, 2003.
9. Jarem, J. M. and P. P. Banerjee, "An exact, dynamical analysis of the Kukhtarev equations in photorefractive barium titanate using rigorous wave coupled wave diffraction theory," *J. Opt. Soc. Amer. A*, Vol. 13, No. 4, 819–831, April 1996.
10. Elsherbeni, A. Z. and M. Hamid, "Scattering by a cylindrical dielectric shell with inhomogeneous permittivity profile," *Int. J. Electronics*, Vol. 58, No. 6, 949–962, 1985.
11. Elsherbeni, A. Z. and M. Hamid, "Scattering by a cylindrical dielectric shell with radial and azimuthal permittivity profiles," *Proc. 1985 Symp. of Microwave Technology in Industrial Development*, 77–80, 22–25, Brazil, (Invited), 1985.
12. Elsherbeni, A. Z. and M. Tew, "Electromagnetic scattering from a circular cylinder of homogeneous dielectric coated by a dielectric

shell with a permitivity profile in the radial and azimuthal directions-even TM case," *IEEE Proceedings-1990 Southeastcon*, Session 11A1, 996–1001, 1990.

13. Jarem, J. M., "Rigorous coupled wave theory solution of phi-periodic circular cylindrical dielectric systems," *Journal of Electromagnetic Waves and Applications*, Vol. 11, 197–213, 1997.
14. Jarem, J. M., " Rigorous coupled wave theory of anisotropic, azimuthally-inhomogeneous, cylindrical systems," *Progress in Electromagnetics Research*, PIER 19, Chap. 4, 109–127, 1998.
15. Jarem, J. M. and P. P. Banerjee, "Bioelectromagnetics: A rigorous coupled wave analysis of cylindrical biological tissue," *Proceedings of the International Conference on Mathematics and Engineering Techniques in Medicine and Biological Sciences*, (METMBS'00), F. Valafar (ed.), 467–472, Vol. II, Las Vegas, Nev., June 26–29, 2000.
16. Jarem, J. M., "Rigorous coupled wave analysis of radially and azimuthally-inhomogeneous, elliptical, cylindrical systems," *Progress In Electromagnetics Research*, PIER 34, 89–115, 2001.
17. Jarem, J. M., "Validation and numerical convergence of the Hankel-Bessel and Mathieu rigorous coupled wave analysis algorithms for radially and azimuthally inhomogeneous, elliptical, cylindrical systems," *Progress In Electromagnetics Research*, PIER 36, 153–177, 2002.
18. Jarem, J. M., "Rigorous coupled-wave-theory analysis of dipole scattering from a three-dimensional, inhomogeneous, spherical dielectric and permeable system," *IEEE Trans. Micowave Theory and Techniques*, Vol. 45, No. 8, 1193–1203, 1997.
19. Jarem, J. M., "A rigorous coupled-wave theory and crossed-diffraction grating analysis of radiation and scattering from three-dimensional inhomogeneous objects," a Letter, *IEEE Transactions on Antennas and Propagation*, Vol. 46, No. 5, 740–741, 1998.
20. Jarem, J. M. and P. P. Banerjee, *Computational Methods for Electromagnetic and Optical Systems*, Marcel Dekker, Inc., N.Y., 2000.
21. Morse, P. M. and H. Feshbach, *Methods of Theorectical Physics*, Chap. 10, 1210–1215, McGraw-Hill Book Company, Inc., N.Y., 1953.
22. Kishk, A. A., R. P. Parrikar, and A. Z. Elsherbeni, "Electromagnetic scattering from an eccentric multilayered circular cylinder," *IEEE Trans. Antennas and Prop.*, Vol. AP-40, No. 3, 295–303, 1992.

23. Churchill, R. V., *Complex Variables and Applications*, McGraw-Hill Book Company, New York, 1960.
24. Abramowitz, M. and I. Stegum, *Handbook of Mathematical Functions*, Chap. 3, "Elementary Analytical Methods", 12, Eq. (3.3.8), Dover publications, New York, N.Y., 1972.
25. Balanis, C. A., *Advanced Engineering Electromagnetics*, 577, Eq. (11-21b), John Wiley & Sons, N.Y., 1989.